A One-Dimensional Hydrodynamic Simulation of Colliding Quasi-Neutral Plasma Systems

A Thesis for the Degree of

Master of Science

By:

Brian Doohan, B.Sc.

National Centre for Plasma Science and Technology

School of Physical Sciences

Dublin City University

Research Supervisor:

Prof. John T. Costello

November 2010

Declaration

I hereby certify that this material, which I now submit for assessment on the programme of study leading to the award of Master of Science is entirely my own work, that I have exercised reasonable care to ensure that the work is original, and does not to the best of my knowledge breach any law of copyright, and has not been taken from the work of others save and to the extent that such work has been cited and acknowledged within the text of my work.

Signed: _____ (Candidate)

ID No.: _____

Date: _____

Table of contents

Abstract

Studies of colliding laser-produced plasmas are of interest in several fields of research, including fusion energy generation, pulsed-laser deposition and potentially as intense short wavelength (X-ray and EUV) light sources. Computer simulations of such systems are a valuable tool in reconciling experimental results with theory and designing new experiments while also providing a platform to explore scenarios which are not easy to realise experimentally.

A one-dimensional (1D) hydrodynamic simulation of quasineutrality-compliant colliding plasma systems has been developed and is described. The model is based on a multi-fluid theory due to P W Rambo and J Denavit [*J. Comput. Phys.* **98** (1992) 317] and uses a flux-corrected transport algorithm with an Eulerian grid in order to solve the three Euler equations for hydrodynamic flow. It includes source terms appropriate for high-density, high-temperature plasmas, such as those produced on dense targets at the focus of intense laser beams. Stagnation and interpenetration effects are simulated by means of collisional momentum coupling between species. Results are compared with the case of colliding plasmas in the absence of collisional coupling.

Chapter 1. Introduction

The study of colliding plasma systems is an area of the physical sciences that has gained momentum in recent years, due to the array of possible technological applications being discovered. Such potential applications include pulsed-laser deposition (PLD) allowing the formation of micro- and nano-structures of high atomic purity and the prospect of colliding plasmas being used as intense extreme ultraviolet (EUV) light sources especially for extreme ultraviolet lithography (EUVL), whereby shorter wavelength light allows for the patterning of smaller-scale structures, vital for the continued increases in semiconductor microchip performance encapsulated in "Moore's Law". Aside from immediate (or short-term) possible technological applications of colliding plasmas, such systems also have the potential to increase our scientific knowledge of atomic processes.

As with all computer simulations of physical processes, the purposes of developing computational models of colliding plasma systems are three-fold: (1) Simulations are performed as an aid in reconciling experimental results with current theoretical understanding, with all three aspects (experimental, theoretical and computational) feeding into and driving the development of new physical understandings; (2) Simulations may suggest new, interesting experiments to perform, since it is most often easier to change the simulation parameters than to re-design experiments repeatedly: a wide range of parameters may be explored in a simulation, with the most potentially revealing simulations studied in experiment; (3) Computer simulations allow for the exploration of situations that may be unattainable experimentally.

1.1 Definition of the plasma state

A plasma is often described simply as an ionised gas. However, a more exact definition of the plasma state is required, since any gas with a non-zero temperature has some degree of ionisation. The Saha equation,

$$\frac{n_i}{n_n} = 2.4\times10^{21}\frac{T^{3/2}}{n_i}e^{(-U_i/kT)} \tag{1.1}$$

describes the fractional ionisation of a gas in *thermal equilibrium*, where n_i and n_n are the densities of the ionised atoms and neutral atoms, respectively, T is the gas temperature, U_i is the ionisation energy of the gas (in eV) and k is Boltzmann's constant. All quantities used in this and the next section will be in SI units, unless otherwise stated. Using the example of air at room temperature, with values of $n_n = 3\times10^{25}\,\mathrm{m}^{-3}$, $T = 300\,\mathrm{K}$ and $U_i = 14.5\,\mathrm{eV}$, gives a fractional ionisation of $n_i/n_n = 10^{-122}$, which, although absurdly small, is nonetheless finite and non-zero [1].

A more descriptive definition of the plasma state is offered by the following statement:

> "*A plasma is a quasineutral gas of charged and neutral particles which exhibits collective behaviour*" [1].

The collective behaviours occur due to the presence of the charged particles and change the dynamics of a plasma system relative to a neutral gas, both in terms of the plasma's reactions to external forces (e.g. applied electric or magnetic potentials) and the possibility of charge separation within the plasma creating electric fields, which in turn modify the dynamics of the system. An example of this latter type of collective effect is ambipolar diffusion. For example, in a system composed of two particle species, singly-ionised atoms and electrons, both species will initially diffuse towards vacuum regions at their thermal velocities,

$$v_s = \sqrt{\frac{kT_s}{m_s}} \tag{1.2}$$

where $s = e$ and $s = i$ for electrons and ions, respectively, and m_s is the mass of species, *s*. The thermal velocity of the electrons is usually much higher than that of the ions, since $m_e << m_i$, resulting in the electrons streaming away from the ions. The resulting charge imbalance, however, simultaneously acts to slow down the electrons and increase the velocity of the ions, thus leading to equilibration of the electron and ion velocities.

To arrive at a more rigorous definition of the plasma state than the statement given above, the concept of *Debye shielding* must be introduced. Consider the example of a pair of charged probes, one positive and one negative, both connected to a battery maintaining their respective polarities, inserted into a plasma. The negative and positive electrodes will quickly attract clouds (sheaths) of ions and electrons, respectively, thereby limiting the effects of the electric fields generated by the electrodes to these regions of charged particles: this is Debye shielding. In a plasma with no thermal energy (i.e. at absolute zero temperature), the shielding would be perfect, since there would be an exactly equal amount of positive and negative charges contained within the sheaths. At a finite temperature, however, the particles at the edges of the clouds are in constant flux, as some of them have enough thermal energy to escape the potential well, and hence the shielding in this case is not perfect [1].

The Debye length is the radius of such a sheath, where the edge is defined to reside at the distance from the electrode where the potential energy due to the applied charge is equal to the thermal energy of the particles, kT, and is given by:

$$\lambda_D \equiv \left(\frac{\varepsilon_0 kT_e}{n_e e^2} \right)^{1/2} \tag{1.3}$$

where ε_0 is the permittivity of free space, T_e and n_e are the electron temperature and density, respectively, and e is the charge of an electron. Contributions to the shielding arising from motions of the ions are neglected in eq. (1.3) since the electrons, being much more mobile than the ions, create the sheaths by moving so as to create a surplus or deficit of negative charges.

A precise distinction between an ionised gas and a plasma consists of three criteria. The first is closely related to the concept of *quasineutrality*; an ionised gas is considered quasineutral if electric potentials are shielded in a distance that is small compared to the plasma spatial dimension, L. That is, if

$$\lambda_D << L \tag{1.4}$$

Another important distinction concerns the number of particles, N_D, contained within a *Debye sphere*, which is the sphere having a radius of the Debye length:

$$N_D = n\tfrac{4}{3}\pi\lambda_D^3 \tag{1.5}$$

where the *plasma density*, $n \cong n_e \cong n_i$, which is valid for systems for which the assumption of quasineutrality is justified [1]. The second criterion that distinguishes an ionised gas from a plasma is, then, that;

$$N_D >> 1 \tag{1.6}$$

since a large number of particles must be present in a Debye sphere for the statistical techniques used in the derivation of the Debye length equation, eq. (1.3), to be legitimate (the derivation is omitted here but may be found in any introductory text on plasma physics, such as refs. [1] and [2]).

The collective behaviour (electromagnetic effects) in a plasma must also dominate the hydrodynamic effects, which are due to collisions involving neutral species, to distinguish it from an ordinary gas. Letting ω denote a representative frequency of plasma oscillations and with τ being

the average time between collisions involving charged species and neutral atoms, then the third criterion for classification of a plasma is

$$\omega\tau > 1 \tag{1.7}$$

In summary, for an ionised gas to qualify as a plasma it must satisfy the three criteria given by eq's. (1.4), (1.6) & (1.7).

The most commonly quoted "representative frequency of plasma oscillations" is the *plasma frequency*, which may be understood by imagining a plasma system, again consisting of two species: ions and electrons. On the relevant timescale, the ions may be thought of as fixed. If some disturbance occurs that causes the electrons to be briefly displaced from their equilibrium positions, then the electrons will move so as to restore the plasma's quasineutrality, but will overshoot and oscillate about the equilibrium positions. The frequency of these oscillations is the plasma frequency, ω_p, and is defined (in Hz) by [3]:

$$\omega_p = \sqrt{\frac{n_e e^2}{m_e \varepsilon_0}} \approx 56.4\sqrt{n_e} \tag{1.8}$$

Figure 1.1 shows the parameter spaces in which a variety of laboratory and naturally-occurring plasmas lie, depicting the huge range of density and temperature values which may be present in plasma.

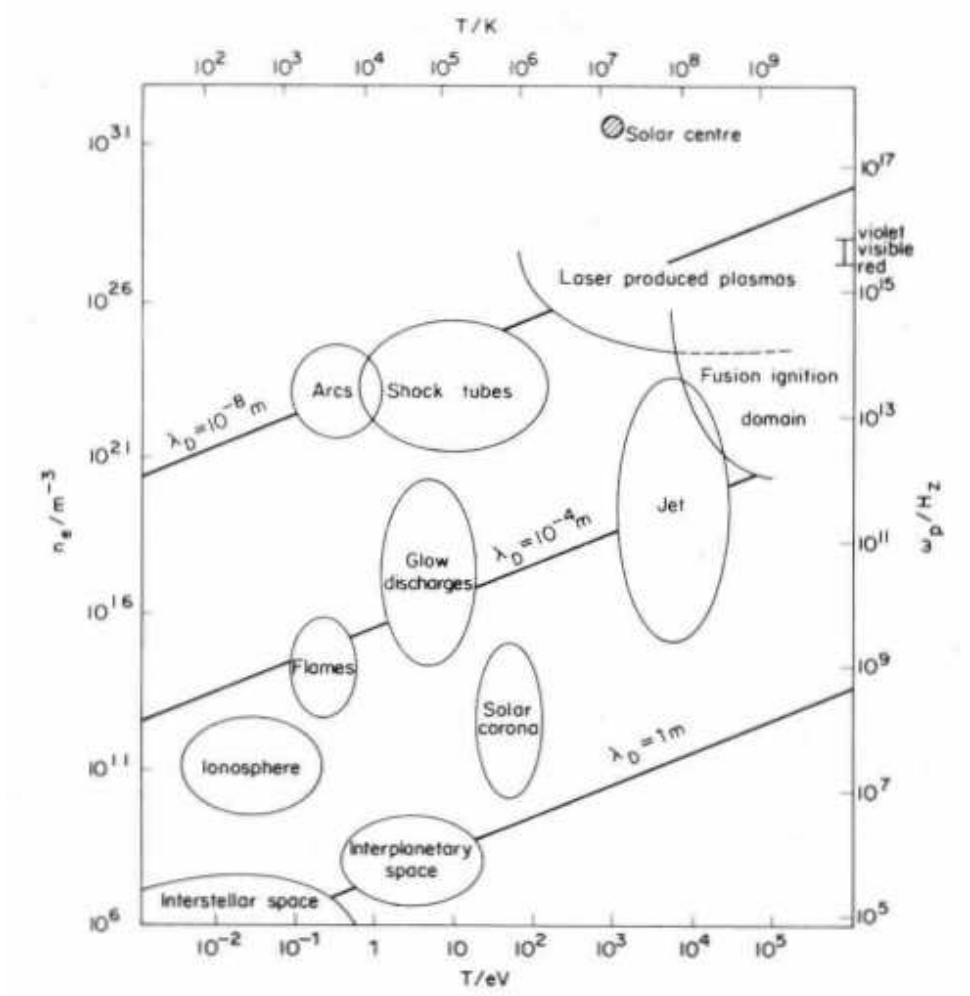

Fig. 1.1: Typical density and temperature ranges for a variety of terrestrial and extra-terrestrial plasmas. Also shown are three Debye lengths and the plasma frequency values. Reproduced from Carroll and Kennedy [3].

1.2 The plasma as a fluid

A typical fluid consists of a large number of atomic or molecular particles, interacting by means of collisions. Thus, the bulk behaviour of a fluid is determined by the aggregation of the distributed behaviour of the constituent elements. In *fluid dynamics* (also known as *hydrodynamics*, the terms will henceforth be used interchangeably), the *continuum assumption* is applied, i.e. the flow variables (density, velocity, pressure etc.) are assumed to vary continuously between infinitesimal fluid elements. The molecular nature of the fluid is ignored; this is in contrast to *kinetic theory*, where the

statistical distribution of the properties of the individual particles is calculated stochastically in order to obtain the bulk properties.

In order for the continuum assumption to be applicable, the system must correspond to the model of *local thermodynamic equilibrium* (LTE). In LTE, electron collisional effects are assumed to dominate and a local electron temperature, T_e, is defined. For LTE to be a justifiable premise, three conditions must be met: (a) the electron velocity distribution is Maxwellian; (b) the populations of ionised species are described by the Saha equations; (c) the populations of excited states are given by the Boltzmann formula; all of which depend on T_e [3]. For LTE to be valid, the electron density must exceed a certain level, given by:

$$n_e \geq 1.6\times10^{18}\sqrt{T_e}\chi^3 \tag{1.9}$$

where χ (in eV) is the excitation potential of the atomic transition in question [3]. A Maxwellian velocity distribution is most commonly attributable to a highly-collisional fluid, however, somewhat surprisingly, even a relatively collisionless plasma may have a velocity distribution that closely approximates a Maxwellian profile [1]. The reason(s) for this phenomenon, first observed by Irving Langmuir in the 1920s and termed *Langmuir's paradox*, is still an open question to this day. Whatever the reason, the fact that a wide range of plasmas display Maxwellian velocity distributions means that the LTE assumptions implied by the hydrodynamic model are justified in most high-density, high-temperature plasmas.

In the definition of other relevant plasma parameters, the concept of the *collisional cross section* must be introduced. If electrons are incident on a slab of neutral atoms, then, upon a collision between an electron and an atom, each electron may lose up to twice its initial momentum (since it may be elastically scattered directly back upon its initial trajectory). The collisional cross section, σ, is defined as the area which could be imagined

to be occupied by each atom if each were totally opaque (perfectly momentum-absorbing) spheres [1].

The *mean free path*, i.e. the average distance travelled between collisions, is given by:

$$\lambda_m = 1/n_n\sigma \tag{1.10}$$

The mean time between collisions, taking the particle velocity to be v, is:

$$\tau = \lambda_m / v \tag{1.11}$$

therefore the average frequency of collisions,

$$\tau^{-1} = v/\lambda_m = n_n\sigma v \tag{1.12}$$

Averaging this quantity in a suitable way over the (Maxwellian) velocity distribution leads to the *collision frequency*, ν:

$$\nu = n_n\overline{\sigma v} \tag{1.13}$$

1.3 The governing equations of fluid dynamics

The governing equations of fluid dynamics are the Navier-Stokes equations, which relate the flow variables (more specifically, the rates of change of the flow variables) for viscous flow. The corresponding relations for inviscid (non-viscous, ideal fluid) flow are the Euler or Lagrange equations. Viscosity is defined as the resistance of a fluid to applied shear and normal stresses. However, in a one-dimensional model, the notion of shear stresses does not apply (see fig. 1.2); therefore, the inviscid assumption is, in general, more physically accurate in a one dimensional scheme than in two or three dimensions.

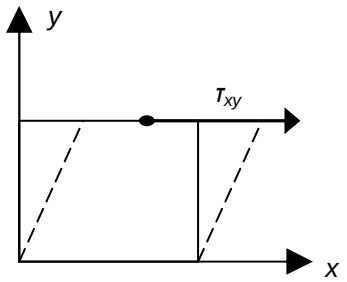

Fig. 1.2: Depiction of shear stress, τ_{xy}, in two dimensions.

Each of the governing equations may be expressed in any one of four distinct, yet equivalent, forms: (a) the differential, conservation form; (b) the differential, non-conservation form; (c) the integral, conservation form; and (d) the integral, non-conservation form (the terms "conservation" and "non-conservation" used here have a different meaning than is usual in Physics literature and will be explained in due course). There are four corresponding theoretical models of the flow (see fig. 1.3), each of which leads directly to one of the forms listed above. The various forms of the governing equations may also be converted between one another by means of mathematical manipulations. The desired form of the Euler equations (the differential, conservation form) will be derived based on the derivations found in ref. [4], adapted where necessary for the one-dimensional case.

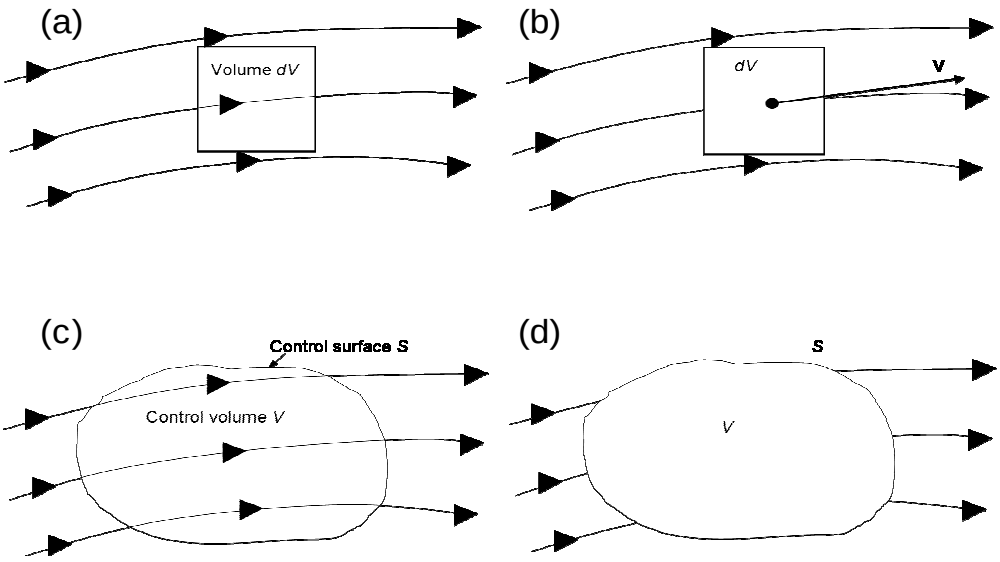

Fig. 1.3: Four theoretical models of the fluid flow. Infinitesimal fluid element fixed in space (a), infinitesimal fluid element moving with the flow (b), finite control volume fixed in space (c), and finite control volume moving with the flow (d).

1.3.1 The continuity equation

Each of the three governing equations of hydrodynamics embodies a fundamental physical principle. The continuity equation arises from the principle of conservation of mass which, when applied to model (a) above, leads to the following statement:

Net mass flow out of dV = time rate of decrease of mass inside dV.

In one dimension, the infinitesimal fluid control volume, dV, becomes an infinitesimal line element, dx. Designating ρ as the density and u as the velocity at spatial coordinate, x, and temporal coordinate, t, the left-hand side of the statement above may be evaluated as follows:

the mass flow *in* through the left of $dx = \rho u$

the mass flow *out* through the right of $dx = \rho u + \frac{\partial(\rho u)}{\partial x} dx$

Therefore,

the net mass flow *out* of $dx = \rho u + \frac{\partial(\rho u)}{\partial x} dx - \rho u$

$$= \frac{\partial(\rho u)}{\partial x} dx \tag{1.14}$$

The right-hand side is simply:

time rate of mass *increase* $= \frac{\partial \rho}{\partial t} dx$

=> time rate of mass *decrease* $= -\frac{\partial \rho}{\partial t} dx$ (1.15)

Equating eq. (1.14) and eq. (1.15):

$$\frac{\partial(\rho u)}{\partial x} dx = -\frac{\partial \rho}{\partial t} dx$$

$$\Rightarrow \boxed{\frac{\partial \rho}{\partial t} + \frac{\partial(\rho u)}{\partial x} = 0} \tag{1.16}$$

Equation (1.16) is the differential, conservation form of the continuity equation in one dimension and is the same for viscous (Navier-Stokes) and inviscid (Euler) flows.

1.3.2 The momentum equation

The physical principle which the momentum equation encapsulates is Newton's second law:

$$F = ma \tag{1.17}$$

In order to derive the momentum equation, this principle will be applied to model (b) of fig. 1.3 above. Since this model is one consisting of an infinitesimal control "volume" moving with the flow, the concept of the *substantial* (or material or Lagrangian) derivative must be introduced. The substantial derivative describes the time rate of change of some physical

quantity at a point (or region) which moves within some time- and/or space-dependent velocity field. As a simple example, consider the situation of a swimmer travelling across a pool which has a temperature gradient held constant in time, e.g. a linear gradient from one, hotter, end of the pool to the other. The time rate of change of temperature at any fixed point in the pool will be zero, however a temperature sensor attached to the swimmer will register a change of temperature as the swimmer moves across the pool. This is analogous to the substantial derivative of the temperature moving with the velocity field of the swimmer. Formally, the substantial derivative is defined as

$$\frac{D\varphi}{Dt} \equiv \frac{\partial \varphi}{\partial t} + \mathbf{V} \cdot \nabla \varphi \equiv \frac{\partial \varphi}{\partial t} + u\frac{\partial \varphi}{\partial x} + v\frac{\partial \varphi}{\partial y} + w\frac{\partial \varphi}{\partial z} \tag{1.18}$$

in three-dimensional Cartesian space, where $\varphi(x, y, z, t)$ is some scalar flow field variable and $\mathbf{V}$ is the velocity field along which the rate of change of φ is measured,

$$\mathbf{V} = u\mathbf{i} + v\mathbf{j} + w\mathbf{k}$$

where $\mathbf{i}$, $\mathbf{j}$ and $\mathbf{k}$ are the unit vectors along the x, y and z axes, and u, v and w are the x, y and z components of velocity, respectively, and are each functions of x, y, z and t.

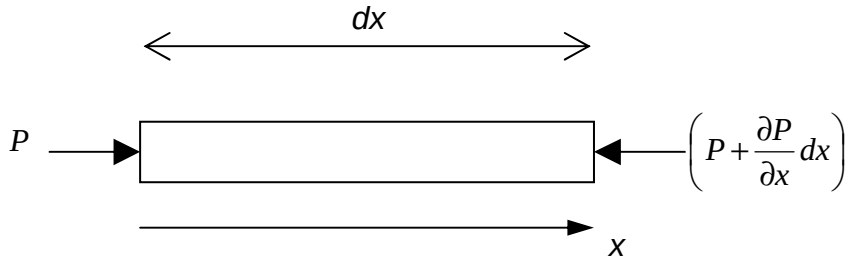

Fig. 1.4: "Surface" forces acting on an infinitesimal fluid element moving with the flow, dx, used in the derivation of the 1-D Euler momentum equation. Fluid element given height for illustrative purposes.

Returning to the application of Newton's second law to the theoretical model being used, the total force experienced by the fluid

element results from forces which fall into one of two general classes: *surface* forces acting on the boundaries of the fluid element and which may vary from one surface to another, e.g. pressure or frictional, viscous forces, and *body* forces acting on the fluid element as a whole, due to, for example, electric or magnetic fields. If viscosity is neglected, the only surface forces acting on a fluid element are those due to pressure (see fig. 1.4). In one dimension, the fluid element in question becomes a line element with length dx. It may be seen that:

the *surface force* acting on the left of $dx = P$

the *surface force* acting on the right of $dx = -\left(P + \frac{\partial P}{\partial x} dx \right)$

where $P = P(x,t)$ is the pressure. If we let $F_b =$ the body force per unit mass, then:

the *body force* acting on fluid element $dx = \rho F_b dx$

Hence, the total force acting on dx,

$$F = \rho F_b dx + P - \left(P + \frac{\partial P}{\partial x} dx \right) = \rho F_b dx - \frac{\partial P}{\partial x} dx \qquad (1.19)$$

which is the left-hand side of eq. (1.17).

Evaluating the right-hand side, the mass is, simply,

$$m = \rho dx \qquad (1.20)$$

and the acceleration,

$$a = \frac{Du}{Dt} \qquad (1.21)$$

Therefore, substituting eq's. (1.19) - (1.21) into eq. (1.17):

$$F = ma$$

$$\Rightarrow \rho F_b dx - \frac{\partial P}{\partial x} dx = \rho dx \frac{Du}{Dt}$$

$$\Rightarrow \rho \frac{Du}{Dt} = -\frac{\partial P}{\partial x} + \rho F_b \qquad (1.22)$$

Equation (1.22) is the differential, non-conservation form of the inviscid momentum equation in one dimension. The meaning of the terms conservation and non-conservation in the context of fluid dynamics may now be explained: by convention, the non-conservation forms of the governing equations are those containing substantial derivative terms, i.e. they are those forms of the equations that are obtained directly from a model of a control volume *moving with the flow*. If the assumption of an inviscid flow is used, as above, then the non-conservation forms may also be referred to as the Lagrange equations. The conservation forms of the governing equations are those which do not include substantial derivative terms. These forms, in the inviscid case, are the Euler equations.

To convert the Lagrangian momentum equation into the desired Eulerian form, we apply the definition of the substantial derivative, eq. (1.18), to the left-hand side of eq. (1.22):

$$\rho \frac{Du}{Dt} = \rho \frac{\partial u}{\partial t} + \rho u \cdot \nabla u \tag{1.23}$$

Applying the product rule of calculus (Leibniz's law):

$$\frac{\partial(\rho u)}{\partial t} = \rho \frac{\partial u}{\partial t} + u \frac{\partial \rho}{\partial t}$$

$$\Rightarrow \rho \frac{\partial u}{\partial t} = \frac{\partial(\rho u)}{\partial t} - u \frac{\partial \rho}{\partial t} \tag{1.24}$$

Using the identity relating to the divergence of a scalar times a vector, taking u as the scalar and (ρu) as the vector:

$$\nabla \cdot (\rho u u) = u \nabla \cdot (\rho u) + (\rho u) \cdot \nabla u$$

$$\Rightarrow \rho u \cdot \nabla u = \nabla \cdot (\rho u u) - u \nabla \cdot (\rho u) = \frac{\partial(\rho u^2)}{\partial x} - u \frac{\partial(\rho u)}{\partial x} \tag{1.25}$$

Substituting eq. (1.24) and eq. (1.25) into eq. (1.23):

$$\rho \frac{Du}{Dt} = \frac{\partial(\rho u)}{\partial t} - u \frac{\partial \rho}{\partial t} + \frac{\partial(\rho u^2)}{\partial x} - u \frac{\partial(\rho u)}{\partial x}$$

$$= \frac{\partial(\rho u)}{\partial t} - u \left[\frac{\partial \rho}{\partial t} + \frac{\partial(\rho u)}{\partial x} \right] + \frac{\partial(\rho u^2)}{\partial x} \tag{1.26}$$

The term in the square brackets in eq. (1.26) above is the left-hand side of the continuity equation, and is thus equal to zero.

$$\therefore \rho \frac{Du}{Dt} = \frac{\partial(\rho u)}{\partial t} + \frac{\partial(\rho u^2)}{\partial x} \tag{1.27}$$

Substituting eq. (1.27) into eq. (1.22) gives:

$$\boxed{\frac{\partial(\rho u)}{\partial t} + \frac{\partial(\rho u^2)}{\partial x} = -\frac{\partial P}{\partial x} + \rho F_b} \tag{1.28}$$

Equation (1.28) is the desired, differential form of the Euler momentum equation in one dimension.

1.3.3 The energy equation

The physical principle which is applied in the case of the energy equation is the first law of thermodynamics: the principle that, in a closed system, energy is conserved. When applied to the model of an infinitesimal control volume moving with the fluid, model (b) of fig. 1.3, it results in the following statement:

Rate of change of energy inside fluid element
= Rate of work done on fluid element + Net heat flux into element

In what follows, we will denote this statement as

$$A = B + C \tag{1.29}$$

The rate of work done by a force on a moving body may be shown to be equal to the product of the force and the component of velocity in the direction of the force [4]. Hence, the rate of work done by the body force on the fluid element is:

$$\rho F_b u dx$$

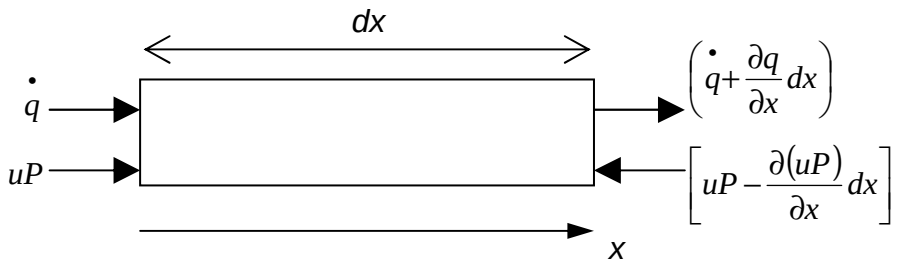

Fig. 1.5: Surface forces and heat fluxes relating to the infinitesimal fluid element moving with the flow, *dx*, for the derivation of the 1-D Euler energy equation. Fluid element given height for illustrative purposes.

Figure 1.5 above illustrates the "surface" forces and heat fluxes acting on the 1-D fluid element under consideration. We will use the convention that forces in the positive x-direction do positive work and vice versa. The net surface force, therefore, is:

$$uP-\left[uP+\frac{\partial(uP)}{\partial x}dx\right]=-\frac{\partial(uP)}{\partial x}dx$$

Then, the quantity B in eq. (1.29) is the sum of the surface and body forces:

$$B=-\frac{\partial(uP)}{\partial x}dx+\rho F_b u dx \tag{1.30}$$

The heat flux into the fluid element is due to two general types of thermal activity: *volumetric heating*, e.g. absorption or emission of radiation and *thermal conduction*, i.e. heat transfer across the surfaces. If we denote the rate of volumetric heating per unit mass as Q_V then, since mass = ρdx, the volumetric heating = $\rho Q_V dx$.

The heat transferred into the fluid element by thermal conduction through both sides is shown in fig. 1.5, where $\dot{q}$ is the heat flux. The net heat conduction is

$$\dot{q}-\left(\dot{q}+\frac{\partial\dot{q}}{\partial x}dx\right)=-\frac{\partial\dot{q}}{\partial x}dx$$

The term C in eq. (1.29) is the sum of volumetric heating and heat conduction:

$$C = \left(\rho Q_V - \frac{\partial \dot{q}}{\partial x} \right) dx$$

From Fourier's law of heat conduction, the heat flux is proportional to the local temperature gradient:

$$\dot{q} = -k \frac{\partial T}{\partial x}$$

where k is the thermal conductivity.

$$\therefore C = \left[\rho Q_V + \frac{\partial}{\partial x} \left(k \frac{\partial T}{\partial x} \right) \right] dx \tag{1.31}$$

On the left-hand side of eq. (1.29), the term A is the time rate of change of the energy of the fluid element. This energy is the sum of the internal energy (the kinetic, thermal, rotational and electronic energies of the atoms or molecules constituting the fluid) per unit mass, U , and the kinetic energy due to the bulk motion of the fluid element as a whole, $u^2/2$ per unit mass. The substantial derivative must be invoked once again, since we are dealing with a fluid element moving with the flow:

$$A = \rho \frac{D}{Dt} \left(U + \frac{u^2}{2} \right) dx \ . \tag{1.32}$$

Combining eq's. (1.29) – (1.32) and dividing both sides by dx:

$$=> \rho \frac{D}{Dt} \left(U + \frac{u^2}{2} \right) = \rho Q_V + \frac{\partial}{\partial x} \left(k \frac{\partial T}{\partial x} \right) - \frac{\partial (uP)}{\partial x} + \rho F_b u \tag{1.33}$$

The conversion of the Lagrange differential form, eq. (1.33), to the differential Euler form proceeds in an equivalent fashion to the manipulations used in the case of the momentum equation and are omitted here. The differential Euler form of the energy equation obtained by conversion of the left-hand side of eq. (1.33) is

$$\boxed{\frac{\partial}{\partial t}\left[\rho\left(U+\frac{u^2}{2}\right)\right]+\frac{\partial}{\partial x}\left[\rho u\left(U+\frac{u^2}{2}\right)\right]=\rho Q_V+\frac{\partial}{\partial x}\left(k\frac{\partial T}{\partial x}\right)-\frac{\partial(uP)}{\partial x}+\rho F_b u} \quad (1.34)$$

Equation (1.34) is the Euler energy equation expressed in terms of the total energy per unit mass, $\left(U+u^2/2\right)$. Equivalent forms of the equation may also be derived expressing the conservation of energy in terms of internal energy, U, alone, or in terms of static enthalpy, h, or total enthalpy, $h_0 = h + u^2/2$. The manipulations involved in these conversions change both sides of the energy equation [4].

The Euler equations of fluid flow in 1-D have now been derived. However, examining the equations reveals that there are four independent flow-field variables (ρ, u, P and e) in only three equations. In order to close the system, the ideal gas equation of state is commonly used:

$$P = \rho RT$$

where R is the specific gas constant. This provides a fourth equation, but also introduces a fifth flow-field variable: the temperature, T. Full closure of the system is accomplished by inclusion of a thermodynamic relation, e.g. the caloric equation of state:

$$e = c_V T$$

where c_V is the specific heat at constant volume.

1.4 Basic computational methods

The Euler equations are a set of partial differential equations (PDEs) for which no closed-form, general analytical solution has been found. The equations describe functions for which variables are required to be defined for the infinite set of continuous values which exist in the domain of interest, e.g. at a certain time, t, each of the flow-field variables (ρ, u etc.) must have a finite, defined value at each of the infinity of spatial positions, x, in the

system's domain. In general, it is not possible to obtain continuous functions describing the variation of these flow-field variables across all times and positions by direct solution of the PDEs.

1.4.1 Discretisation (finite differencing)

Discretisation is the process by which the continuous functions represented by an equation are replaced by analogous approximate, algebraic relations defined only at discrete temporal and/or spatial positions (grid points). The procedure of discretisation of PDEs is termed *finite difference* discretisation or "the method of finite differences".

The simplest finite difference discretisations are based on Taylor series expansions. If u_i is the velocity at spatial position, *i*, then the velocity at $i+1$, u_{i+1}, may be expressed in terms of a Taylor series expansion about point *i*, as follows:

$$u_{i+1} = u_i + \left(\frac{\partial u}{\partial x}\right)_i \Delta x + \left(\frac{\partial^2 u}{\partial x^2}\right)_i \frac{(\Delta x)^2}{2} + \left(\frac{\partial^3 u}{\partial x^3}\right)_i \frac{(\Delta x)^3}{6} + \ldots \tag{1.35}$$

which is an exact expression for u_{i+1} in the limit of an infinite number of terms in the Taylor series.

Solving eq. (1.35) for $\left(\partial u / \partial x\right)_i$ gives:

$$\left(\frac{\partial u}{\partial x}\right)_i = \frac{u_{i+1} - u_i}{\Delta x} - \left(\frac{\partial^2 u}{\partial x^2}\right)_i \frac{\Delta x}{2} - \left(\frac{\partial^3 u}{\partial u^3}\right)_i \frac{(\Delta x)^2}{6} + \ldots \tag{1.36}$$

Equation (1.36) may be rewritten in the form,

$$\boxed{\left(\frac{\partial u}{\partial x}\right)_i = \frac{u_{i+1} - u_i}{\Delta x} + O(\Delta x)} \tag{1.37}$$

where $O(\Delta x)$ represents the *truncation error* associated with the finite difference approximation of $\left(\partial u / \partial x\right)_i$.

Because the truncation error includes a term of Δx to the first power, then the finite difference represented by eq. (1.37) is termed *first-order*

accurate. Furthermore, since the finite difference contains only u_{i+1} and u_i, i.e. no terms to the left of point *i*, then it is called a *forward* difference.

A first-order accurate, *backward* difference discretisation is found by writing a Taylor series for u_{i-1} expanded about u_i:

$$u_{i-1} = u_i + \left(\frac{\partial u}{\partial x}\right)_i (-\Delta x) + \left(\frac{\partial^2 u}{\partial x^2}\right)_i \frac{(-\Delta x)^2}{2} + \left(\frac{\partial^3 u}{\partial x^3}\right)_i \frac{(-\Delta x)^3}{6} + \ldots \qquad (1.38)$$

which, when solved for $\left(\partial u / \partial x\right)_i$, as above, gives:

$$\boxed{\left(\frac{\partial u}{\partial x}\right)_i = \frac{u_i - u_{i-1}}{\Delta x} + O(\Delta x)} \qquad (1.39)$$

To obtain a *second-order* accurate finite difference, we can construct a Taylor series for $u_{i+1} - u_{i-1}$ by subtracting eq. (1.38) from eq. (1.35):

$$u_{i+1} - u_{i-1} = 2\left(\frac{\partial u}{\partial x}\right)_i \Delta x + 2\left(\frac{\partial^3 u}{\partial x^3}\right)_i \frac{(\Delta x)^3}{6} + \ldots$$

$$=> \boxed{\left(\frac{\partial u}{\partial x}\right)_i = \frac{u_{i+1} - u_{i-1}}{2\Delta x} + O(\Delta x)^2} \qquad (1.40)$$

Since the finite difference includes information from grid points on both sides of *i*, eq. (1.40) is a second-order accurate, *central* difference expression.

It is evident that there exists a large number of finite difference discretisations which may be derived (limited only by the number of grid points in the domain), of increasing order of accuracy, incorporating the values at a greater number of grid points. For example, a fourth-order accurate central difference approximation for the first derivative is:

$$\left(\frac{\partial u}{\partial x}\right)_i = \frac{u_{i-2} - 8u_{i-1} + 8u_{i+1} - u_{i+2}}{12(\Delta x)} + O(\Delta x)^4$$

Increasing the order of accuracy is desirable, since it naturally results in a more accurate solution, may give sharper shocks and, for a required level of accuracy needs fewer grid points. However, there are also disadvantages: computing time is increased at each grid point due to more calculations being performed, larger matrices being stored, etc. and programming challenges, especially near boundaries (to be discussed in the following subsection).

Much of the impetus for the past investigations into CFD came from the need for aerodynamicists to accurately model, for example, air flow over aircraft designs. In many of these types of simulations a *steady-state* solution is ultimately sought. However, often this is only possible by modelling the unsteady solution to long timescales at which convergence to the steady state is obtained. The method of stepping through time is known as *time-marching*, and is performed by calculating all the flow variables across the entire spatial domain at each time-step before the simulation moves on to the next time-step. The types of unsteady, inviscid flow involved in plasma simulations require time-marching solutions.

The choice of discretisation method is generally a trade-off between numerical accuracy within smooth regions and accuracy near discontinuities, such as those found at shocks, expansion fans and contacts, at which the formal order of accuracy may drop to first-order (or lower) for even high-order methods. Sophisticated discretisation schemes have been developed to combat the limitations of particular methods, e.g. by using a weighted average of different discretisations, which are modified automatically depending on the "steepness" of the solution about a point. See chapters 17, 18 & 20-23 of ref [5] for a detailed analysis of the relative strengths and weaknesses of a large variety of both simple and more advanced discretisation schemes.

To end this discussion of basic discretisation methods, we will briefly mention the other two main types of discretisation. *Finite volume* methods, instead of using samples as the primary representation of a function, as is the case for finite difference methods, use cell-integral averages as the primary representation of a function. Thus, they are most often used to approximate integral equations. *Finite element* methods differ by constructing "piecewise-polynomial" representations of a function, i.e. they approximate a functions' value at each cell by a polynomial interpolation between neighbouring samples.

1.4.2 Boundary treatments

For an inviscid, one-dimensional model of fluid flow with *solid* (non-porous) walls, the only *physical* boundary condition to be enforced is that there is no mass transfer into the wall, i.e. the velocities at the walls are zero. This is referred to as the "no-penetration boundary condition". The values of the other flow-field variables at the walls are generated by the numerical solution to the governing equations. The *numerical* implementation of the no-penetration condition can be accomplished by using one of a variety of boundary treatments.

Any single finite difference scheme will suffer from a lack of available samples at one or both boundaries. For example, a backward-difference at the left boundary requires the use of point $i-1$ which, when $i=1$, is the point 0 and is outside the computational domain. A central difference will have this problem at both boundaries. One method of resolving this issue is by changing the finite difference scheme used at the problematic boundary, e.g. if a first-order backward difference is being used for the interior solution then, at cell $i=1$, a forward difference may be used to ensure the samples needed lie within the computational domain. Second- and higher-order differences can be derived that are *one-sided*, that is they contain only grid

points on one side of *i*. An example of a second-order, one-sided forward finite difference is:

$$\left(\frac{\partial u}{\partial x}\right)_i = \frac{-3u_i + 4u_{i+1} - u_{i+2}}{2\Delta x} + O(\Delta x)^2$$

An alternative to changing the finite difference at the boundary is to use the idea of *ghost cells*, also known as the "reflection boundary condition". This boundary treatment, in order to cope with the lack of available grid points at a boundary, generates the necessary grid points for the finite difference by using the condition that the first cell *outside* the domain has the same values for the flow-field variables as the last cell *inside* the domain (except the velocity, which has the same magnitude, but opposite sign), the second cell outside equates to the second-last cell inside and so on, until all the grid points needed have been generated. This method ensures that the variables are continuous across the boundary, however discontinuities commonly occur in the first derivative across the boundary, which may lead to spurious oscillations, overshoots etc., as at any discontinuity.

The two boundary treatments briefly described above are both examples of *solid* boundaries. *Far-field* or *permeable* boundaries are another class of boundary treatments that, instead of reflecting the fluid back towards the interior, may both absorb and emit fluid out of or into the computational domain. These types of treatments are more complicated than solid boundaries, as information must be inferred where there is no explicit data computed. Therefore, whereas solid boundaries impose only *physical* conditions on the fluid flow at a boundary, far-field boundaries are purely *numerical* in origin and involve using a number of additional assumptions. Far-field boundaries are typically used where a steady-state solution is sought, e.g. aerodynamic simulations.

1.4.3 CFL condition, artificial viscosity

The Courant-Friedrichs-Lewy (CFL) condition, also commonly known as the Courant condition, is an important criterion that must be satisfied at all times and positions in any numerical solution of PDEs. The CFL condition is that the Courant number,

$$C = u_{\max} \frac{\Delta t}{\Delta x} \leq 1 \tag{1.41}$$

This condition simply states that for any given time-step, the maximum velocity must not be greater than that which would allow fluid to travel more than one grid-step. Simulations where the Courant number exceeds one generally become unstable and quickly "blow up", e.g. values grow rapidly and uncontrollably. Often, these problematic simulations may be run successfully by reducing the time-step, with the concomitant increase in computing time.

The Euler equations, as has been described previously in section 1.3, are inviscid approximations to the Navier-Stokes equations. The Navier-Stokes momentum equation in conservation form, with "standard assumptions such as Stokes' hypothesis and Fourier's law for heat transfer" [5] applied, is:

$$\frac{\partial(\rho u)}{\partial t} + \frac{\partial}{\partial x}\left(\rho u^2 + P\right) = \frac{\partial}{\partial x}\left(\frac{4}{3}\mu \frac{\partial u}{\partial x}\right)$$

where μ is the coefficient of viscosity. The right-hand side, the viscous term, is a second derivative term and arises from *physical* viscosity. Physical viscosity makes a fluid system more stable by damping small oscillations caused by small disturbances.

While the Euler equations omit viscosity considerations, many discretisations re-introduce *viscous-like* terms in the form of second-differences, analogous to the second derivative terms in the Navier-Stokes

equations. These second differences may arise naturally from certain differencing schemes, for example the second-order forward difference,

$$\left(\frac{\partial u}{\partial x}\right)_i = \frac{-u_{i+2} + 4u_{i+1} - 3u_i}{2\Delta x} + O(\Delta x)^2$$

may be re-written as a first difference plus a second difference;

$$\left(\frac{\partial u}{\partial x}\right)_i = \frac{u_{i+1} - u_i}{\Delta x} - \frac{u_{i+2} - 2u_{i+1} + u_i}{2\Delta x} + O(\Delta x)^2$$

Other times, second differences may be intentionally added to first-derivative approximations. Regardless of how they originate, these viscous-like terms have no direct relationship to physical viscosity, i.e. they are purely numerical in origin, and are thus termed *artificial* viscosity. The advantage of artificial viscosity is increased stability; often a method requires artificial viscosity to be added explicitly to prevent it from becoming unstable, however this benefit comes at the cost of decreased accuracy [4]. Thus, one must be careful about when and how much artificial viscosity should be used.

1.5 Summary

The chapter began by defining the plasma state. In words, the three conditions that must be met are: (a) the distance over which local electric fields are shielded from the bulk of the plasma, due to Debye shielding, must be much less than the size of the plasma; (b) the number of particles contained within a sphere having a radius of the Debye length must be large for the concept of Debye shielding to be statistically valid; (c) collective, electromagnetic effects, due to the interactions of the charged particles, must dominate ordinary hydrodynamic effects, due to collisions involving neutral atoms.

In section 1.2, it is described that the Maxwellian velocity distribution, characteristic of highly collisional gases, is approached to a

high degree of accuracy in many plasmas, even among those that may be said to be collisionless. This is termed Langmuir's paradox and, although the causes are still largely unknown, the result is that the fluid model of plasmas is applicable in most cases and is able to describe the majority of experimentally-observed plasma phenomena.

The derivation of the one-dimensional, inviscid governing equations of hydrodynamics, the 1D Euler equations, is detailed in section 1.3. These equations arise from the application of fundamental physical laws (mass conservation, Newton's second law, energy conservation) to theoretical models of the fluid flow, by examining the various fluxes crossing the surfaces of the idealised control "volumes" (in the 1D case, these volumes are line elements), together with the forces acting on these surfaces.

In section 1.4, the basics of the numerical methods employed to solve the Euler equations (and other partial differential equations) are presented. The numerical technique of finite differencing is first introduced and examples of forward, backward and centred discretisations of first- and second-order of accuracy are given. A brief discussion of boundary treatments then follows, together with descriptions of two of the most important considerations affecting numerical discretisations: the CFL condition and artificial viscosity.

Chapter 2. The Rambo & Denavit model of colliding plasmas

2.1 Model outline

The hydrodynamic model of Rambo and Denavit was initially developed for the simulation of isothermal and adiabatic plasma-vacuum expansion tests and published in 1991 in ref. [6]. This two-fluid (ions and electrons), collisionless model was a one-dimensional fluid dynamics model defined on a uniform Eulerian grid, using a modified version of the Boris and Book flux-corrected transport (FCT) method [7-9] for the differencing scheme by which the Euler equations are solved. FCT is a relatively sophisticated transport algorithm, incorporating a flux-limiter, involving solution-sensitive limited application of an anti-diffusive flux to the values predicted by a low-order diffusive flux. The successful coupling of the fluid dynamics algorithm to an electric field (Poisson equation) solver was demonstrated. However, in this present work, electric field considerations have been omitted. The numerical tests of ref. [6] were designed to verify the acceptable behaviour of the fluid and field algorithms at the fluid-vacuum boundary, and all results published were given in terms of dimensionless, normalised units.

In ref. [10], the algorithms developed by Rambo and Denavit in ref. [6] were generalised to include collisional forces between multiple atomic species (ions, neutrals, electrons) in the form of collisional momentum coupling, temperature equilibration and heat conduction between species. In this formulation, interpenetration and stagnation effects, present in physical colliding plasma experiments, may be simulated. The numerical tests presented apply the model to a variety of scenarios, showing acceptable behaviour in the simulation of Ohmic heating, a friction test resulting in a shock at the interface between two fluids, colliding plasmas displaying interpenetration, and plasma shocks involving two fluids (ions and electrons). All results were again given in terms of normalised units.

2.2 Detailed technical description

2.2.1 Staggered grid

In ref. [6], Rambo and Denavit take great pains to describe the effect of changing the locations on the grid where the various flow variables are sampled and the fluxes are calculated. The two basic possibilities are: (a) to define quantities at cell centres, i, or (b) to define them at cell edges, $i \pm ½$. Accurate discretisation schemes can be defined on either type of grid, however the grid that they found to produce the most reliable results is a *mixed* grid type, largely to accommodate electric field (Poisson equation) solver problems, but also to help stability in the electric-field-free cases such as those studied here. It was deemed prudent to follow the formulation adopted by Rambo and Denavit to allow for easier incorporation of an electric field solver, should the code be extended at a later stage.

The final grid scheme adopted by Rambo and Denavit, which they refer to as "Scheme #3", defines densities, temperatures and momenta at cell centres and velocities at cell edges. Because the specific electric field solver they used required the averaging of velocities in adjoining cells, velocities defined at cell centres, investigated in "Scheme #1", led to unphysical *even-odd* oscillations in the velocity profiles when the electric field solver was turned on (see figs. 4 & 5 of ref [6]).

2.2.2 Flux-corrected transport: density transport

The original flux-corrected transport (FCT) method was developed by Boris and Book and first published in 1973 [7]. It is an example of a "predictor-corrector" method, whereby the values at the new time-step are calculated by a *two-step procedure* from the values at the previous time-step. This will be illustrated by using the example of density transport. The first

step involves the application of a low-order, *diffusive* flux, f^L, to obtain temporary densities,

$$n_j^{TD} = n_j^0 - \left(f_{j+1/2}^L - f_{j-1/2}^L \right) \tag{2.1}$$

Here, the subscripts indicate the spatial position on the grid, where *j* is a cell centre and $j \pm ½$ are cell edges, while the superscripts (except for the "*L*" superscript which simply identifies the fluxes as the low-order fluxes) specify the time-level, where *0* signifies values at the previous time-step and *t* indicates values at the new time-step. The temporary densities obtained by eq. (2.1) are then "corrected" by limited application of a higher-order, *antidiffusion* flux, f^A:

$$n_j^t = n_j^{TD} - \left(C_{j+1/2} f_{j+1/2}^A - C_{j-1/2} f_{j-1/2}^A \right) \tag{2.2}$$

where the *flux limiter*, *C*, is defined by

$$C_{j+1/2} = \sigma . Max\left(0,\ Min\left\{ \sigma\left(n_{j+2}^{TD} - n_{j+1}^{TD}\right),\ \left| f_{j+1/2}^A \right|,\ \sigma\left(n_j^{TD} - n_{j-1}^{TD}\right) \right\}\right) \tag{2.3}$$

where $\sigma = Sign\left(f_{j+1/2}^A\right)$. Equation (2.3) is constructed so as to allow as much of the high-order flux to be restored as possible, without creating or intensifying maxima or minima, what Laney terms the "range-diminishing" condition, see section 16.3 of ref. [5].

What is missing from the above discussion is the definition of the fluxes in question. The original FCT method used the SHASTA transport algorithm [7], however this type of transport requires all quantities to be cell-centred. In 1979, Zalesak [11] generalised the Boris and Book FCT method to allow for a wide range of first- and second-order differences to be used. With the velocities defined at cell edges, Rambo and Denavit describe the use of several differencing possibilities for the low-order and antidiffusion fluxes. The method they demonstrated to give the best results in the single-fluid vacuum expansion tests for Scheme #3 is what they refer to as "FCT-Fromm" advection. This method uses "Donor Cell" as the low-order flux:

$$f^{L}_{j+1/2} = \varepsilon_{j+1/2} n^{0}_{j} \qquad \text{for} \qquad \varepsilon_{j+1/2} \geq 0$$

$$= \varepsilon_{j+1/2} n^{0}_{j+1} \qquad \text{for} \qquad \varepsilon_{j+1/2} < 0 \tag{2.4}$$

and Fromm's method [12] for the antidiffusion flux:

$$f^{A}_{j+1/2} = \frac{1}{4}\varepsilon_{j+1/2}\left(1-\varepsilon_{j+1/2}\right)\left(n^{0}_{j+1} - n^{0}_{j-1}\right) \qquad \text{for} \qquad \varepsilon_{j+1/2} \geq 0$$

$$= -\frac{1}{4}\varepsilon_{j+1/2}\left(1+\varepsilon_{j+1/2}\right)\left(n^{0}_{j+2} - n^{0}_{j}\right) \qquad \text{for} \qquad \varepsilon_{j+1/2} < 0 \tag{2.5}$$

where $\varepsilon_{j+1/2} = \dfrac{\Delta t}{\Delta x} u_{j+1/2}$ is the local CFL number.

The equations (2.1) - (2.5) allow advancement of the density from the previous to the new time-step. The operator, Ψ, we will use as shorthand to denote a single step of the transport algorithm. The density transport then may be represented by the expression:

$$n^{t}_{j} = \Psi\left\{n^{0}_{j}, u^{t}_{j+1/2}\right\} \tag{2.6}$$

It may be noted that eq. (2.6) involves the use of velocities at the new time-step, $u^{t}_{j+1/2}$, however this implies introducing an implicit method into the algorithm. Due to programming challenges, in this work these velocities are approximated by using the velocities from the previous time-step, u^{0}, thereby keeping the transport method fully explicit (except in the case of the collisional momentum coupling, see subsection 2.2.4).

2.2.3 Energy and momentum transport

The transport algorithms for momentum and energy involve the same relations as those involved in the density transport, with the densities, n_j, in eq's. (2.1) - (2.6) replaced by $(nu)_j$ and $(nT)_j$, in the case of momentum and energy, respectively. However, an important difference is

the necessary inclusion of source term contributions to model the effects of pressure gradients within the gas or quasineutral plasma.

The internal (thermal) energy of the fluid, $U = 3nT/2$, thus allowing the energy transport to be accomplished by means of advancing the temperature in a suitable manner. Including the pressure source term, one step of the temperature transport is described by the equation:

$$T_j^t = \frac{1}{n_j^t}\Psi\left[n_j^0 T_j^0, u_{j+1/2}^t\right] - \frac{2}{3}\Delta t \frac{P_j^t}{n_j^t}\frac{u_{j+1/2}^t - u_{j-1/2}^t}{\Delta x} \tag{2.7}$$

where the pressure,

$$P_j = n_j T_j + Q_j \tag{2.8}$$

with the artificial viscosity, Q, necessary to give stable solutions in compressive regions, defined by

$$\begin{aligned} Q_j &= 0 && \text{for} \quad u_{j+1/2} \geq u_{j-1/2} \\ &= \kappa m n_j \left(u_{j+1/2} - u_{j-1/2}\right)^2 && \text{for} \quad u_{j+1/2} < u_{j-1/2} \end{aligned}$$

where m is the particle mass and κ is a dimensionless quantity, typically set to unity (as in all results to be presented later in this work), used to adjust, if required, the strength of the artificial viscosity.

The momentum and velocity transport requires multiple steps, since the momenta and velocities are defined at different positions on the grid. First, the momenta are advanced from the momenta at the previous time-step:

$$(nu)_j^* = \Psi\left\{(nu)_j^0, u_{j+1/2}^t\right\}. \tag{2.9}$$

Intermediate velocities at the cell boundaries are then calculated by an averaging of the momenta in the adjoining cells:

$$u_{j+1/2}^* = \frac{1}{2}\left[\frac{(nu)_j^*}{n_j^t} + \frac{(nu)_{j+1}^*}{n_{j+1}^t}\right] \tag{2.10}$$

The intermediate velocities then have the source terms applied, giving the velocities at the new time-level:

$$u^t_{j+1/2} = u^*_{j+1/2} + \Delta t\left[-\frac{1}{m\left\langle n^t\right\rangle_{j+1/2}}\,\frac{P^t_{j+1}-P^t_j}{\Delta x}\right]$$

$$\equiv u^*_{j+1/2} + \Delta u_{j+1/2} \tag{2.11}$$

where $\langle n\rangle_{j+1/2}$ is the average of the densities in cells *j* and *j+1*.

To complete the momentum transport, the momenta are then advanced by an average of the source terms from the cell edges:

$$(nu)^t_j = (nu)^*_j + \tfrac{1}{2} n^t_j\left(\Delta u_{j+1/2} + \Delta u_{j-1/2}\right) \tag{2.12}$$

2.2.4 Collisional momentum coupling

All of the equations (2.1) – (2.12) are applicable to single-fluid models, that is they do not include references to atomic species. In their 1992 paper [10], Rambo and Denavit generalise the transport algorithms to include multiple species. In this multi-fluid formulation, the set of equations (2.1) – (2.12) are repeated for each species. The notation is to replace all flow-field variables measured at specific grid positions by values at these grid positions *for each species*. For example, eq. (2.6) re-written to include multiple species becomes:

$$n^t_{s,\,j} = \Psi\left\{n^0_{s,\,j}, u^t_{s,\,j+1/2}\right\}$$

with the extra subscript, *s*, referring to the specific species in question.

The interaction between species in this work is by means of collisional momentum coupling. The collisionless momentum transport equations, eq's. (2.9) – (2.10), are first applied to each species individually, with eq. (2.11) applied in a re-stated form to give the collisionless velocities,

$$u_{s,j+1/2}^{coll-less} = u_{s,j+1/2}^{*} + \Delta t\left[-\frac{1}{m_s \left\langle n^t \right\rangle_{s,j+1/2}} \frac{P_{s,j+1}^t - P_{s,j}^t}{\Delta x} \right] \tag{2.13}$$

The collisionless velocities obtained by eq. (2.13) then have the collisional source terms applied:

$$u_{s,j+1/2}^t = u_{s,j+1/2}^{coll-less} - \Delta t\left[\sum_{s'} \frac{m_{ss'}}{m_s} \nu_{ss'} \left(u_s^t - u_{s'}^t \right) \right]_{j+1/2} \tag{2.14}$$

where m_s is the mass of species, s, $\nu_{ss'}$ is the collision frequency between species, s and s', and $m_{ss'} = m_s m_{s'} / \left(m_s + m_{s'} \right)$.

The right-hand side of eq. (2.14) uses velocities at the new time-level to calculate the collisional coupling between the species, requiring that the set of equations represented by eq. (2.14) be solved simultaneously for each species at the cell edge, $j + \frac{1}{2}$, to maintain stability. This is accomplished by using the following equation to update the collisionless velocities:

$$u_{s,j+1/2}^t = \left[\mathbf{A}_{ss'} \right]^{-1} \left[u_{s,j+1/2}^{coll-less} \right] \tag{2.15}$$

where the collisional momentum coupling matrix at $j + \frac{1}{2}$,

$$\mathbf{A}_{ss'} = \begin{bmatrix} 1 + \sum_{s' \neq 1} \Delta t \frac{m_{1s'}}{m_1} \nu_{1s'} & -\Delta t \frac{m_{12}}{m_1} \nu_{12} & \cdots \\ -\Delta t \frac{m_{21}}{m_2} \nu_{21} & 1 + \sum_{s' \neq 2} \Delta t \frac{m_{2s'}}{m_2} \nu_{2s'} & \cdots \\ \cdots & \cdots & \cdots \end{bmatrix} \tag{2.16}$$

The source term contributions are then added to the momenta, completing the momentum transport:

$$\left(nu \right)_{s,j}^t = \left(nu \right)_{s,j}^{*} + \tfrac{1}{2} n_{s,j}^t \left(\Delta u_{s,j+1/2} + \Delta u_{s,j-1/2} \right) \tag{2.17}$$

where

$$\Delta u_{s,j+1/2} = u_{s,j+1/2}^t - u_{s,j+1/2}^{*}$$

is the total source term contribution to the velocity at $j + \frac{1}{2}$.

The definition of the collision frequencies, ν, used by Rambo and Denavit in the colliding plasma simulations of [10] is:

$$\nu_{ss'} = \frac{1}{\eta d} \frac{n_{s'}}{m_{ss'}^{1/2} T_{ss'}^{3/2}} \tag{2.18}$$

where

$$T_{ss'} = m_{ss'} \left[\frac{T_s}{m_s} + \frac{T_{s'}}{m_{s'}} \right]$$

and $d = j_{\max} \Delta x$ is the scale length. Equation (2.18) is a simplified expression for the collision frequencies, one that does not depend on the relative streaming velocities of the species in question. The dimensionless *collisionality parameter*, η, is inversely proportional to the collision frequency and approximately equal to the ratio of the mean-free-path to the scale length [10].

To complete the collisional coupling between species, the collision frequencies and new velocities are used in an additional temperature source term to model dissipation. The "new" temperatures obtained by eq. (2.7) are modified in the following manner:

$$T_{s,j}^{(1)} = T_{j,s}^{t} + \tfrac{1}{2} \left\{ \delta T_{j+1/2} + \delta T_{j-1/2} \right\}_s \tag{2.19}$$

where

$$\delta T_{s,j+1/2} = \frac{2}{3} \Delta t \sum_{s'} \frac{m_{ss'}^2}{m_s} \left[\nu_{ss'} (u_s - u_{s'})^2 \right]_{j+1/2}^{t} \tag{2.20}$$

The Rambo and Denavit collisional model also includes temperature equilibration and heat conduction between species, however these considerations have not yet been included in this work.

2.3 Summary

In this chapter, the inner workings of the Rambo and Denavit hydrodynamic model have been described, in the absence of electric fields, for both the single-fluid and multi-fluid formulations.

The single-fluid model is defined on a mixed Eulerian grid type, with densities, temperatures, pressures and momenta defined at cell centres, and velocities defined at cell edges. At each time-step, densities are first updated from the previous time-step by application of a low-order, diffusive flux (Donor cell), which are then corrected by limited application of a higher-order, antidiffusion flux (Fromm's method). A similar procedure is implemented in the transport of the other primitive variables, velocities and temperatures, with the necessary inclusion of source term (pressure gradient) contributions in each case. The velocity transport has the extra complication of momenta and velocities being defined at different positions on the spatial grid, which is resolved by transporting the momenta at each time-step, with the new velocities (at cell edges) defined by suitably averaging the momenta in the two adjacent cells.

The multi-fluid model first applies the single-fluid transport algorithms to each species separately. The coupling between species is accomplished by: (a) the use of an additional source term in the momentum transport equation (collisional momentum coupling), involving a collisional momentum coupling matrix having elements dependent on the relative masses of the particles and the collision frequencies between the particle species in question; (b) an additional temperature source term to model dissipation, with corrections to the predicted temperatures dependent on the relative masses, the collision frequency and the relative streaming velocities of the particular species.

Chapter 3. Results – Numerical tests and comparisons

3.1 Numerical accuracy tests: comparisons with analytical solutions

The initial numerical accuracy tests performed with the code described in the previous chapter are exactly as outlined in ref. [6]. These simulations are "applicable to a neutral gas, or to a single fluid plasma model obeying quasineutrality" [6], and involve isothermal and adiabatic expansions into vacuum. All results in this chapter are given in terms of dimensionless, normalised quantities: the characteristic length is λ_0; density is measured relative to the characteristic density, n_0; velocity, particle mass and temperature are given in units of v_0, m_0 and T_0, respectively, and are related by $v_0 = \sqrt{T_0/m_0}$ (the thermal velocity relation); and a unit of time, $t_0 = \lambda_0/v_0$. At time $t = 0$, a region of undisturbed fluid of length x_0 and density $n = n_0$ is present at the left side of the system, with a vacuum region extending from the fluid-vacuum interface to the right boundary.

3.1.1 Isothermal vacuum expansion tests- qualitative comparisons

The first test is an isothermal simulation, with the temperature held constant at $T = T_0$. A self-similar solution exists for this problem, making it an ideal test case for the purpose of validating the numerical accuracy of the computational model. The self-similar solution is given by [6]:

$$\left.\begin{array}{c} n = \exp(-1-\eta) \\ u = 1+\eta \end{array}\right\} \qquad \text{for} \quad \eta = \frac{(x-x_0)}{C_s t} > -1 \tag{3.1}$$

where $C_s = v_0$ is the isothermal sound speed. Spatial positions for which $\eta < -1$ are regions of undisturbed fluid, with $n = n_0$ and $u = 0$. The isothermal tests are initialised at time $t = t_0$ with the density and velocity profiles as given by eq. (3.1) with $x_0 = 50\Delta x$. The total system length is

$200\Delta x$, with $\Delta x = \lambda_0$. The initial density and velocity profiles, together with the resulting initial momentum, are shown in fig. 3.1.

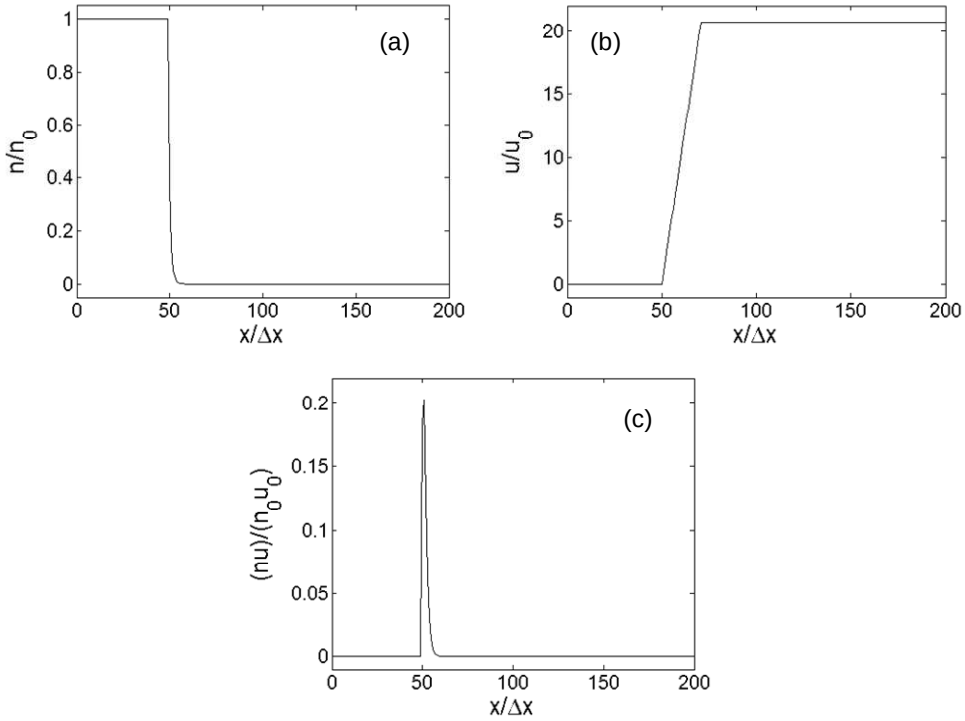

Fig. 3.1: Initial profiles for isothermal vacuum expansion test. Self-similar density (a), velocity (b) and resulting momentum (c) at time $t = t_0$.

Figure 3.2 shows the density, velocity and momentum from a simulation with $\Delta t = 0.025 t_0$ at time $t = 6t_0$, i.e. after 200 time-iterations. The computed results are shown in solid lines while the self-similar, analytical solutions are plotted in dashed lines. The velocity successfully attains its maximum value, $u_{\max} = \ln\left(n_0 / n_{floor}\right) = 20.7$, in the vacuum region and only small deviations from the analytical solutions are visible in the plots.

Figure 3.3, a snapshot of the same simulation at a later time, t=8.5 (300 time-iterations), reveals improved agreement with the analytical solutions, as is particularly evident upon comparing the momentum plots, fig. 3.2(c) and fig. 3.3(c).

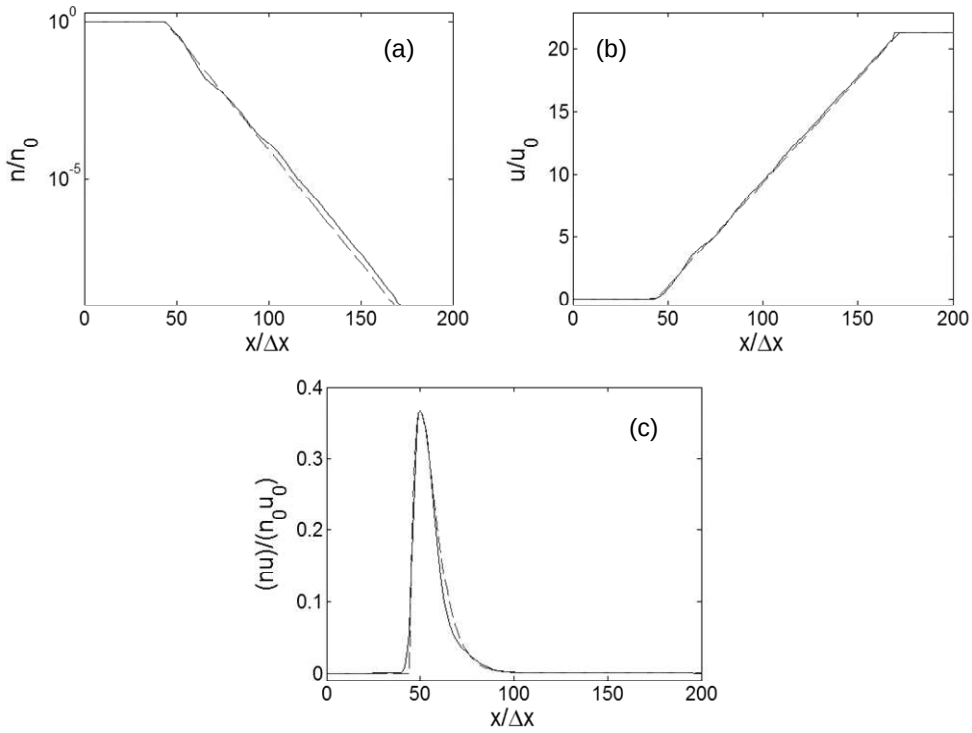

Fig. 3.2: Isothermal vacuum expansion test. Density (a), velocity (b) and momentum (c) at time $t = 6t_0$; $\Delta t = 0.025t_0$, after 200 time-steps.

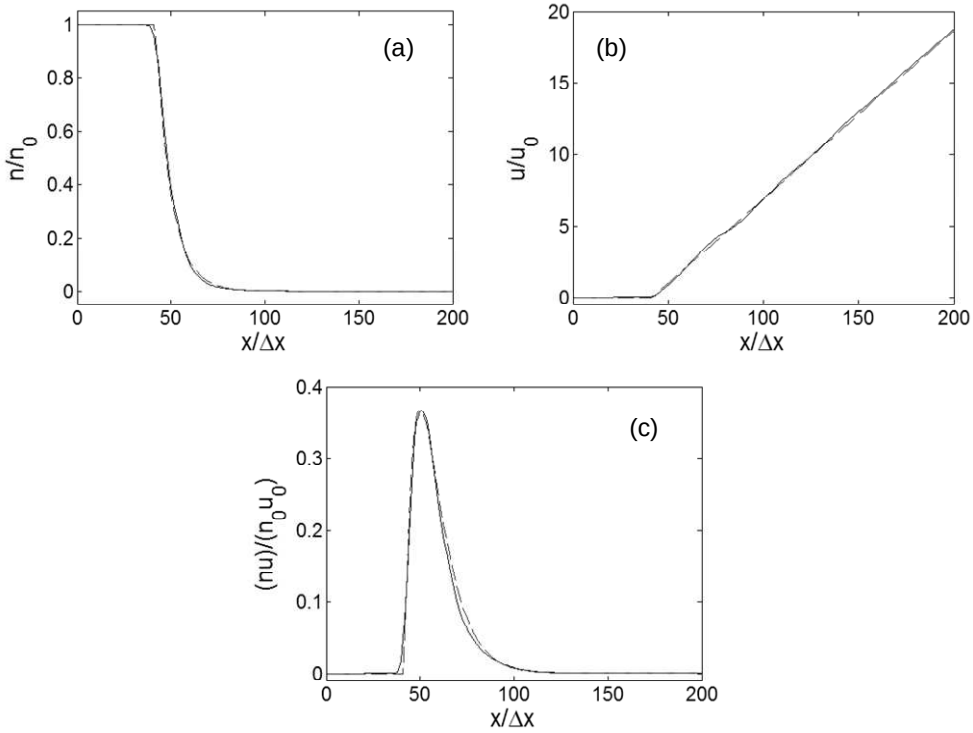

Fig. 3.3: Isothermal vacuum expansion test. Density (a), velocity (b) and momentum (c) at time $t = 8.5t_0$; $\Delta t = 0.025t_0$, after 300 time-steps.

3.1.2 Adiabatic vacuum expansion tests- quantitative comparisons

The next test is an adiabatic (constant total thermal energy) test with temperature variations included. Again, a self-similar solution to this problem exists, with the density, velocity and temperature profiles given by:

$$n = \frac{(3-\xi)^3}{4^3}$$
$$u = \frac{3C_a(1+\xi)}{4} \qquad \text{for} \quad -1 < \xi < 3 \tag{3.2}$$
$$T = \frac{(3-\xi)^2}{4^2}$$

where

$$\xi = \frac{(x - x_0)}{C_a t}$$

For a monatomic ideal gas ($\gamma = 5/3$), the adiabatic sound speed, $C_a = \sqrt{\gamma} = 1.29 v_0$. Values of x for which $\xi < -1$ are regions of undisturbed fluid, with $n = T = 1$ and $u = 0$, while $\xi > 3$ corresponds to the vacuum region, where $n = T = 0$ and the velocity, $u = u_{\max} = 3C_a$ [6].

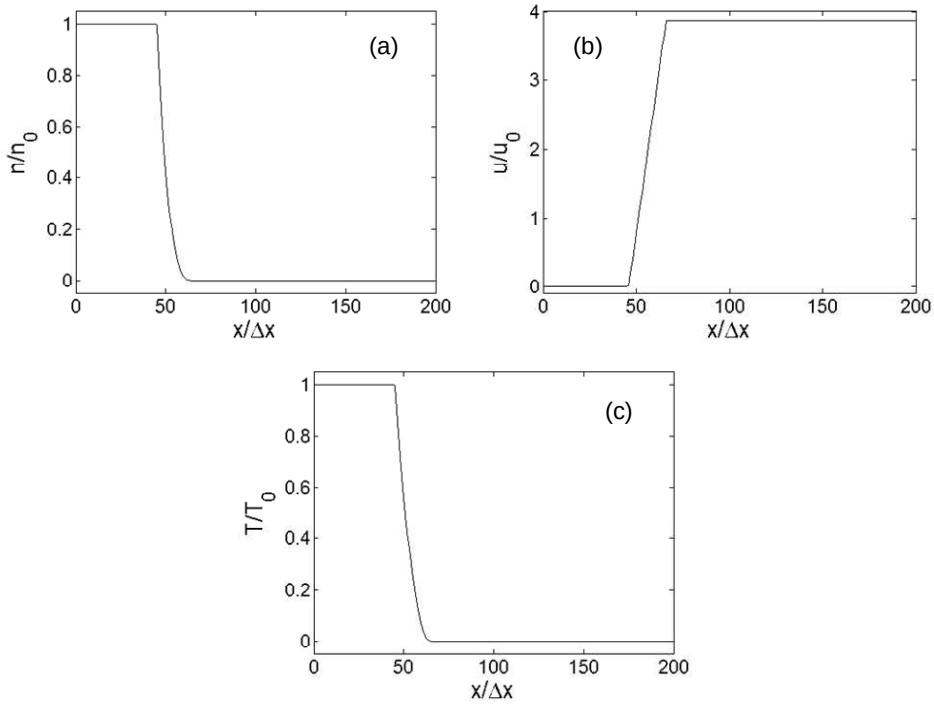

Fig. 3.4: Initial profiles for adiabatic vacuum expansion test. Self-similar density (a), velocity (b) and temperature (c) at time $t = 3.88 t_0$.

The adiabatic tests are initialised according to the self-similar solutions at time $t = 3.88t_0$; the initial profiles are shown in fig. 3.4. Again, $x_0 = 50\Delta x$, the total system length is $200\Delta x$ and $\Delta x = \lambda_0$.

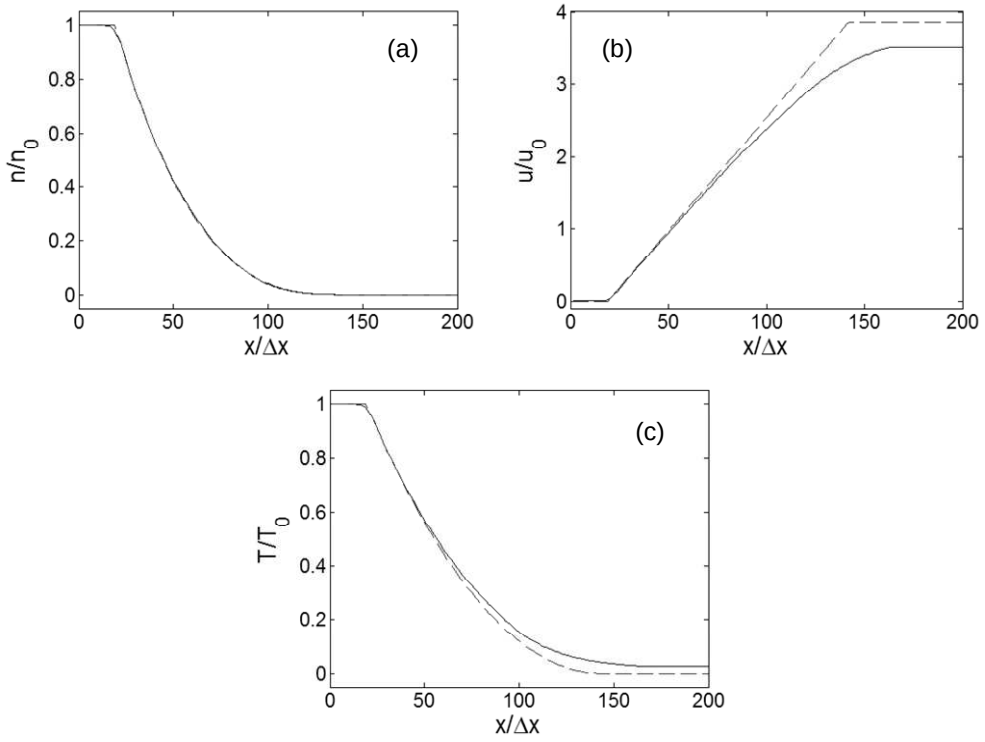

Fig. 3.5: Adiabatic vacuum expansion test. Density (a), velocity (b) and temperature (c) at time $t = 23.88t_0$; $\Delta t = 0.1t_0$, after 200 time-steps.

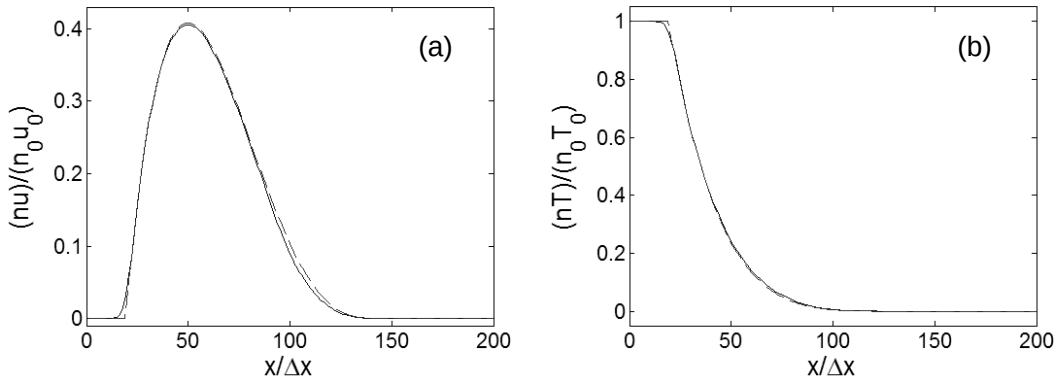

Fig. 3.6: Adiabatic vacuum expansion test. Momentum (a) and pressure (b) at time $t = 23.88t_0$; $\Delta t = 0.1t_0$, after 200 time-steps.

Figures 3.5 and 3.6 show the results from the simulation at time $t = 23.88t_0$, with $\Delta t = 0.1t_0$ (200 time-iterations), compared to the analytical predictions. From fig. 3.5(a), it can be seen that the computed density profile is almost indistinguishable from the theoretical values, although the velocities and temperatures diverge from the analytical solutions near the fluid-vacuum interface, figs. 3.5(b) and 3.5(c), respectively. The plots of momentum and pressure, figs. 3.6(a) and 3.6(b), show excellent agreement with theory, however, since the deviations in velocity and temperature occur in regions of low density.

For a quantitative analysis of the accuracy of the solutions, we will use a widely-accepted measure of the agreement between computed solutions and expected solutions, the *normalised root mean square deviation* (NRMSD). If we take $\alpha(x)$ to be the analytical values and $\beta(x)$ as the computed values of some flow-field variable, then the formula to calculate the NRMSD (expressed as a percentage) is;

$$err(\beta) = \frac{100}{(\alpha_{\max} - \alpha_{\min})} \sqrt{\frac{\sum_{x=1}^{j_{\max}} [\alpha(x) - \beta(x)]^2}{j_{\max}}} \tag{3.3}$$

where $j_{\max}$ is the total system length (in terms of Δx).

Applying eq. (3.3) to the plots of momentum and pressure of fig. 3.6, the calculated errors are $err(nU) = 1.30\%$ and $err(nT) = 0.428\%$, respectively.

Similar to the isothermal case, letting the simulation run to longer times improves the agreement between computation and theory as evidenced by fig. 3.7, which is a snapshot of the same simulation at the later time $t = 33.88t_0$ (300 time-iterations). The density remains almost indistinguishable from the analytical solution, while the deviations visible in the velocity and temperature plots have decreased, with the computed values approaching the theoretical values in the vacuum region. The

momentum and pressure profiles of fig. 3.8 again show good agreement, with average percentage errors of $err(nU) = 1.19\%$ and $err(nT) = 0.421\%$, respectively.

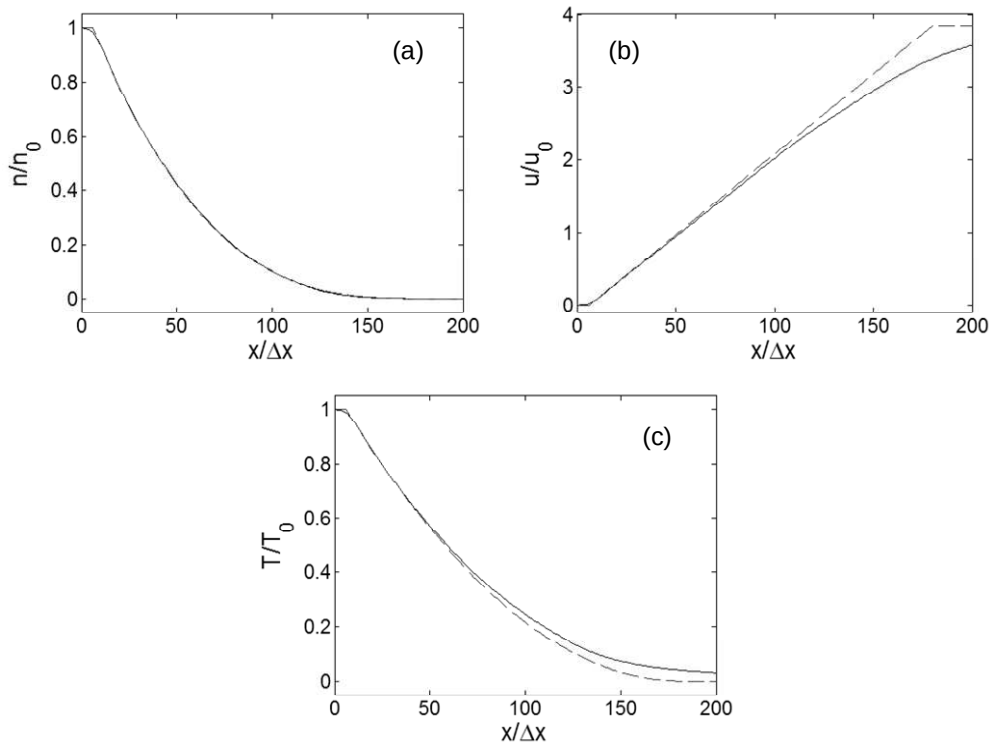

Fig. 3.7: Adiabatic vacuum expansion test. Density (a), velocity (b) and temperature (c) at time $t = 33.88t_0$; $\Delta t = 0.1t_0$, after 300 time-steps. $\varepsilon_{\max} = 0.36$.

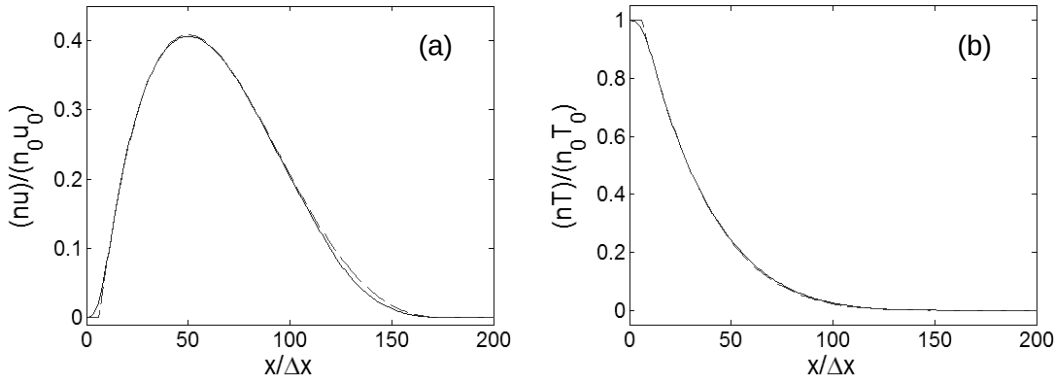

Fig. 3.8: Adiabatic vacuum expansion test. Momentum (a) and pressure (b) at time $t = 33.88t_0$. Parameters as for fig 3.7.

With $\Delta t = 0.1t_0$, the maximum Courant number attained in the simulation, $\varepsilon_{\max} = 0.36$. Such a low value has two disadvantages: the computation time is increased due to the increased number of time-steps required to cover a given time-interval and the effect of round-off errors is compounded due to the greater number of calculations being performed per unit time. A second adiabatic simulation was carried out with a larger time-step, $\Delta t = 0.25t_0$, with all other parameters as before, leading to a maximum Courant number, $\varepsilon_{\max} = 0.98$. Results from this simulation at time $t = 33.88t_0$ are presented in figs. 3.9 and 3.10. Improved agreement is again visible in the plots, borne out by the average percentage error values in this case of $err(nU) = 1.14\%$ and $err(nT) = 0.348\%$.

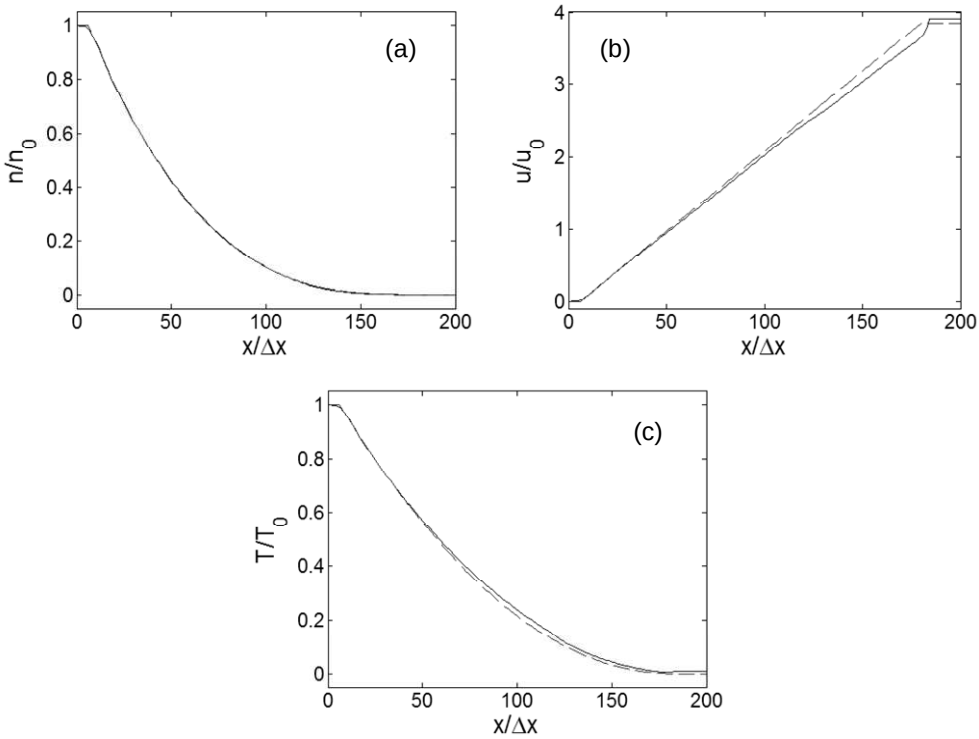

Fig. 3.9: Adiabatic vacuum expansion test #2. Density (a), velocity (b) and temperature (c) at time $t = 33.88t_0$; $\Delta t = 0.25t_0$. $\varepsilon_{\max} = 0.98$.

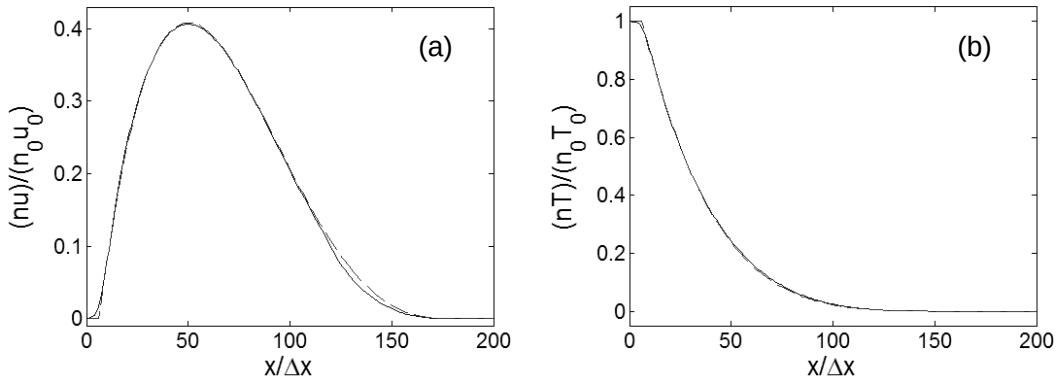

Fig. 3.10: Adiabatic vacuum expansion test #2. Momentum (a) and pressure (b) at time $t = 33.88t_0$. Parameters as for fig. 3.9.

3.2 Colliding quasi-neutral plasma simulations

In this section, we will apply the computational models (single fluid and multi-fluid) to simulations of colliding quasi-neutral plasmas. All results are again given in terms of normalised units, as described in the previous section. The simulations detailed here do not possess analytical solutions, thus quantitative measurements of the accuracy of the results are not possible in this case. However, all tests will be initialised as close as is feasible, in the absence of electric field and electron fluids, to the colliding plasma simulations presented in Rambo and Denavit's 1992 paper [10]. This will allow qualitative comparisons between the data presented here and that presented in ref. [10]: where a figure in this section has a direct analogue in the work of Rambo and Denavit, the relevant figure is here reproduced from ref. [10] for direct comparison.

The colliding plasma simulations of this section involve two plasma slabs, with trapezoidal density profiles of full-width at half-maximum of $20\Delta x$, separated by a distance of $110\Delta x$, as shown in fig. 3.11. When comparing the plots given here with the analogous results of ref. [10], it may be noted that the spatial axes are different, spanning the region $200\Delta x < x \leq 400\Delta x$ in the plots presented here, contrary to the corresponding figures from Rambo and Denavit that span the region $0 < x \leq 200\Delta x$. This is due to the required use of "buffer" regions, of minimum length $200\Delta x$, on either side of the system to move the simulation boundaries away from the central, collisional region. From examination of simulations without these buffer regions it was ascertained that, although not directly mentioned in ref. [10], the simulations of Rambo and Denavit also included such a removal of the boundaries away from the collisional region. In the absence of these buffer regions, build-ups of temperature and density will accumulate at each boundary, causing several undesirable boundary effects such as the interaction of the diffusing fluid with the high-pressure cells near the walls leading to shocks propagating back towards the centre of the system.

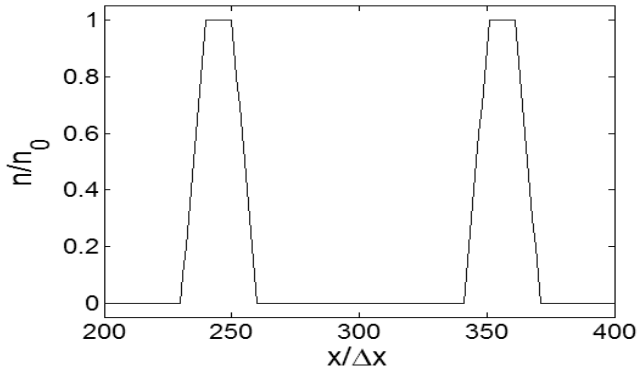

Fig. 3.11: Initial density profile of the colliding plasma slabs.

3.2.1 Single fluid colliding plasma simulation

The single fluid simulation has density initialised as in fig. 3.11, with a particle mass of $m = 100m_0$, an initial temperature of $T = 1.1T_0$ and a spatial grid-step of $\Delta x = \lambda_0$. With a time-step of $\Delta t = 0.5t_0$, fig. 3.12 shows the density and temperature profiles at times $t = 240t_0$ and $t = 600t_0$. At $t = 240t_0$, the slabs have come into contact at the centre of the system and begun to stagnate, leading to compression of the fluid on both sides of the collision plane, as the diffusing fluid encounters the high-temperature, high-pressure fluid at the collision interface. At $t = 600t_0$, as more fluid has moved towards the centre and stagnated, outward-propagating shocks are visible, together with the effect of the high-pressure central region in forcing rarefaction and diffusion of the fluid away from the centre.

Comparing fig. 3.12 with the analogous results published by Rambo and Denavit, presented here as fig. 3.13, it is evident that the two sets of results agree closely, with the exception that the central, peak temperatures are greater in fig. 3.13. The reason for this perplexing difference remains an open question, since both single fluid simulations are initialised identically and both computational models incorporate the same transport algorithms, source terms etc. In this author's opinion, the most likely cause of the discrepancy is a difference in the handling of the temperature transport in vacuum regions.

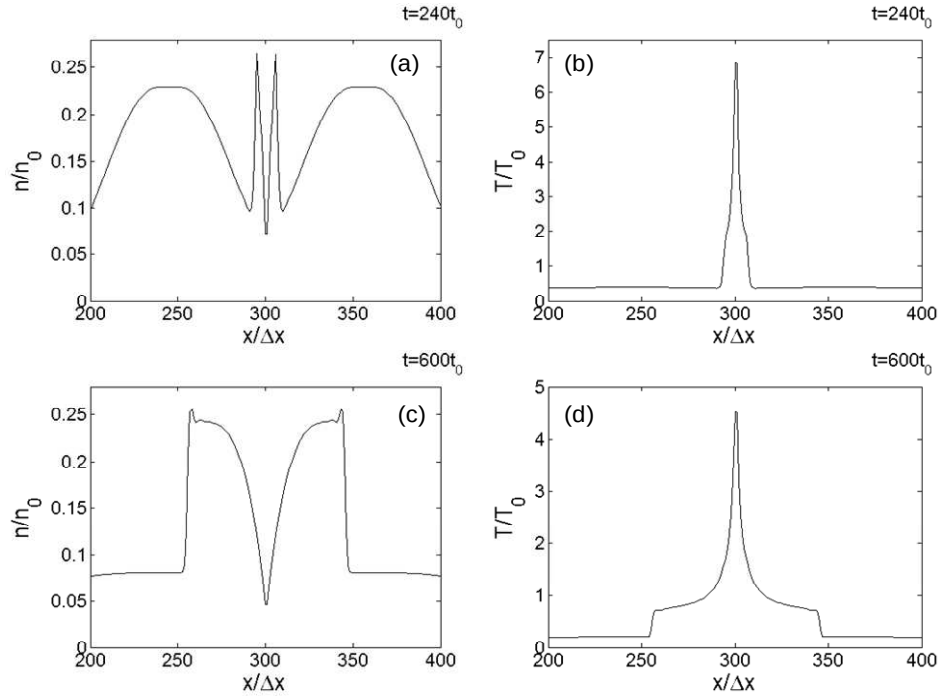

Fig. 3.12: Single fluid colliding plasma simulation. Density (a) and temperature (b) at time $t = 240t_0$; density (c) and temperature (d) at time $t = 600t_0$. $\Delta t = 0.5t_0$.

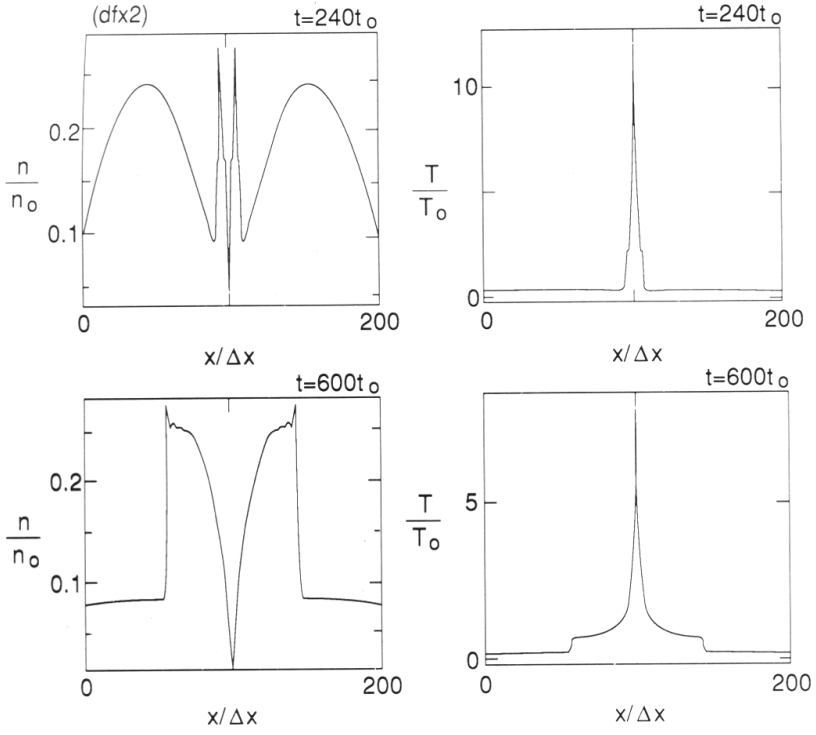

Fig. 3.13: Results from Rambo & Denavit's single fluid colliding plasma simulation. Parameters as in fig. 3.12. Reproduced from ref. [10].

The evolution of the density and temperature profiles are shown in figs. 3.14 and 3.15, respectively. At $t = 120t_0$, the leading edges of the expansions have come into contact at the centre of the system, see fig. 3.14(a), resulting in a high-temperature spike, see fig. 3.15(a).

From $t = 360t_0$ to $t = 600t_0$, the strong outward-propagating shocks become visible, together with the cooling of the fluid behind the shocks, see figs. 3.15(c) and 3.15(d). In the density plot at $t = 360t_0$, fig. 3.14(c), the shocks appear as sharp discontinuities, with the peak density values on either side of the collision plane dropping from values of $n \approx 0.45n_0$ to $n \approx 0.1n_0$ in three cells. This shows that the model exhibits only a small degree of numerical *smearing*, which is a desirable property of any numerical solution containing discontinuities. Behind the shocks (i.e. towards the centre), dispersion-like oscillations in the density values may be noted, spanning regions of approximately eight cells each. These oscillations are numerical effects and are undesirable consequences of many numerical solutions to PDEs in the presence of shocks [5]. Examining the similar regions just behind the shocks in the density plots at later times, $t = 480t_0$ and $t = 600t_0$, figs. 3.14(d) and 3.12(c), respectively, these oscillations are shown to diminish in both amplitude and in the sizes of the affected regions, converging to smoother representations of the fluid elements immediately behind the shocks.

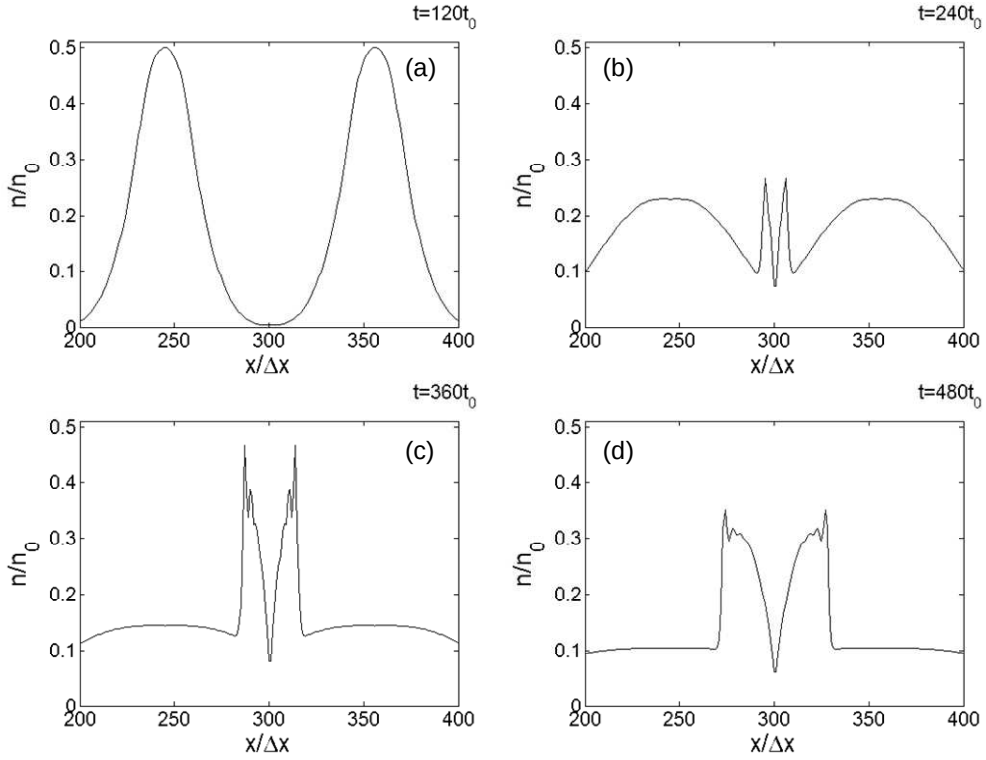

Fig. 3.14: Single fluid colliding plasma simulation. Density profiles at times $t = 120t_0$ (a), $t = 240t_0$ (b), $t = 360t_0$ (c) and $t = 480t_0$ (d). $\Delta t = 0.5t_0$.

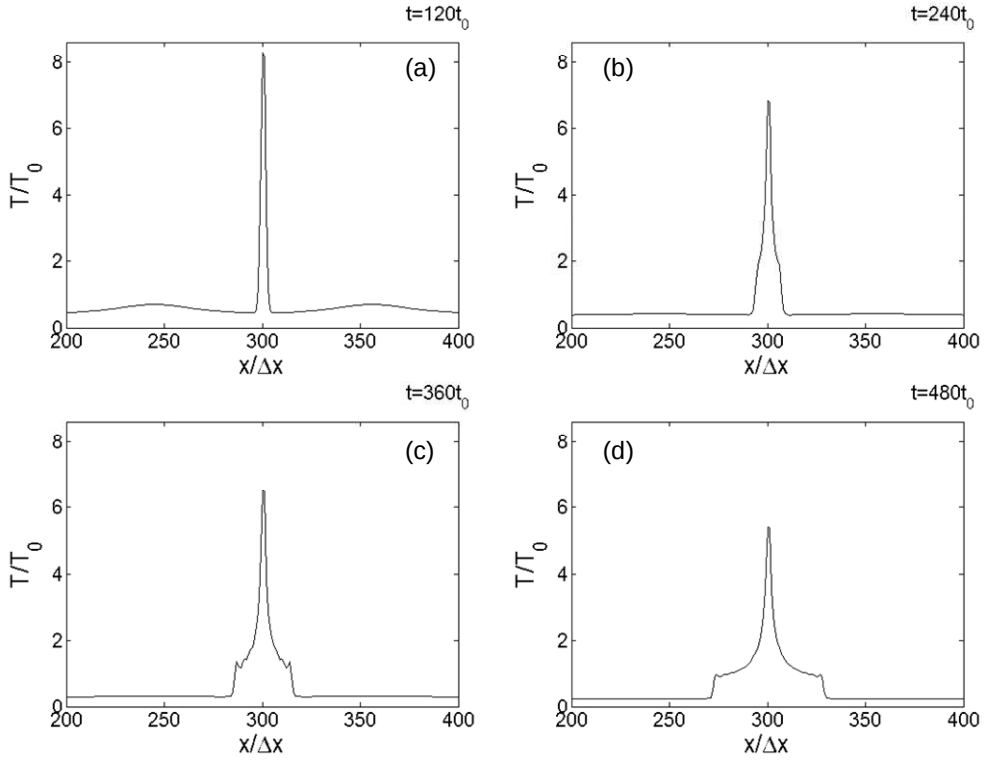

Fig. 3.15: Single fluid colliding plasma simulation. Temperature profiles at times $t = 120t_0$ (a), $t = 240t_0$ (b), $t = 360t_0$ (c) and $t = 480t_0$ (d). $\Delta t = 0.5t_0$.

Snapshots of the momenta and pressures at two times, $t = 240t_0$ and $t = 600t_0$, are shown in fig. 3.16. Early evidence of the presence of the shocks appears at $t = 240t_0$, in both the momentum and pressure plots of figs. 3.16(a) and 3.16(b). From the differences in the shocks' positions between times $t = 240t_0$ and $t = 600t_0$, the average speed with which the shocks are propagating outwards is found to be $v_{shock} = 0.53v_0$. The numerical oscillations behind the shocks are again revealed in the pressure plot at time $t = 240t_0$, fig. 3.16(b), and are shown to have smoothed out significantly by time $t = 600t_0$, see fig. 3.16(d).

Of note in the momentum plots at times $t = 240t_0$ and $t = 600t_0$ is the reversal of the fluid flow between the two times induced by the high-pressure at the centre pushing fluid away; compare figs 3.16(a) and 3.16(c). Another interesting feature revealed by the momentum plots is the reversal of the direction of shock propagation. Limiting one's attention to the region to the left of the midplane, justified since the momentum plots are antisymmetric about the midplane, the shock in fig. 3.16(a), visible as a sharp discontinuity centred around position $x = 294\Delta x$, has positive momentum, indicating that it is travelling to the right, towards the centre. The analogous discontinuity at time $t = 600t_0$, located at $x \approx 256\Delta x$ in fig. 3.16(c), has negative momentum, indicating that it is now propagating to the left, away from the centre. Again, this is due to the effect of the high-pressure central cells in preventing diffusion of fluid into, or across, the midplane.

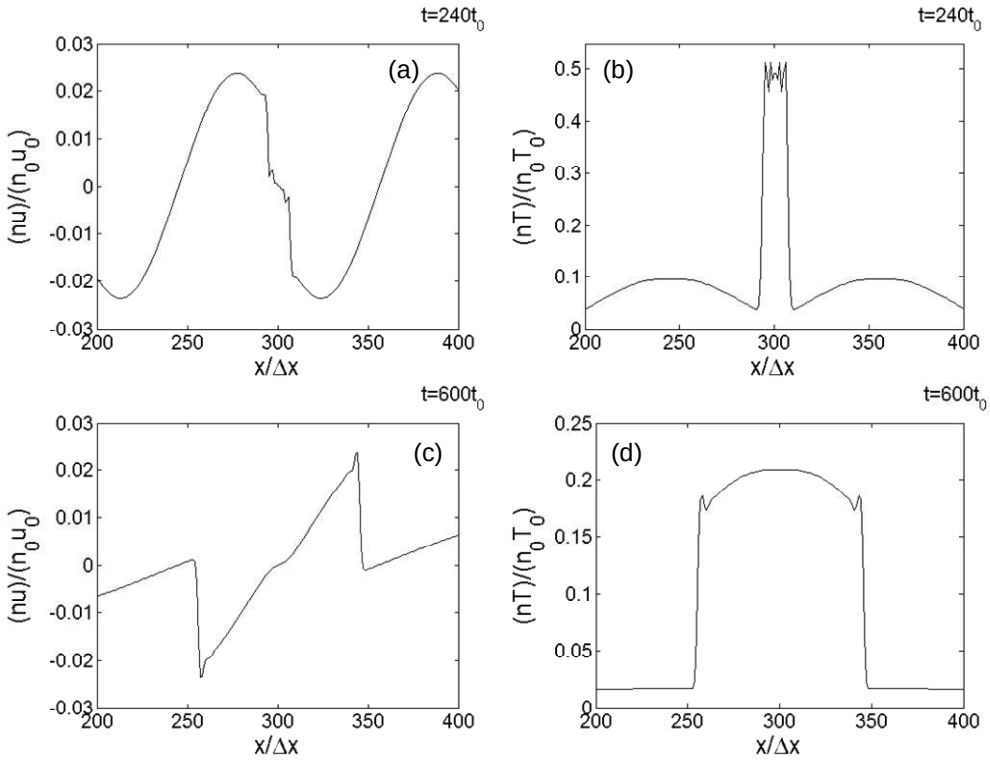

Fig. 3.16: Single fluid colliding plasma simulation. Momentum (a) and pressure (b) at time $t = 240t_0$; momentum (c) and pressure (d) at time $t = 600t_0$. $\Delta t = 0.5t_0$.

3.2.2 Multi-fluid simulations with collisional momentum coupling

The multi-fluid simulations also have density initialised according to the profile shown in fig. 3.11, with the exception that the two plasma slabs consist of different, distinct, but identical neutral atomic fluids: the left slab is fluid 1 and the right slab is fluid 2. The two fluids will interact by means of collisional momentum coupling, as described in subsection 2.2.4. There are several ways in which the simulations presented here differ from the analogous simulations presented in ref. [10]. The most important difference is the absence in this work of electric field considerations and electron fluids. Other omissions concern the temperature transport algorithms where, in this work, temperature equilibration and thermal conduction between species have not yet been incorporated. Thus, direct comparisons with the

multi-fluid results published by Rambo and Denavit reveal poorer agreement than in the tests presented to this point.

The particle mass is $m = 100m_0$, the initial temperature is $T = 1.1T_0$ and the spatial grid-step is $\Delta x = \lambda_0$, all identical to the values used in the single fluid colliding plasma simulation, while the time-step used here, $\Delta t = 0.2t_0$. The first simulation, simulation #1, has the *collision parameter*, $\eta = 6.8 \times 10^{-3}$. Snapshots of the densities of each of the two fluids (dashed lines) and the total density (solid lines), $n_{tot} \equiv n_1 + n_2$, together with the average temperature, $T_{av} \equiv \left(n_1 T_1 + n_2 T_2\right)/n_{tot}$, are shown in fig. 3.17 at two times, $t = 240t_0$ and $t = 600t_0$.

Comparing fig. 3.17 with the analogous results presented in ref. [10], included here as fig. 3.18, several differences may be noted, due to the reasons previously described. Examining the two sets of plots at $t = 240t_0$, it may be seen that, up to this time, the diffusion of the plasma plumes has proceeded almost identically in both cases. However, the plots of the temperature at this time are vastly different: where a temperature spike is visible in fig. 3.18, fig. 3.17(b) shows an almost flat temperature profile. In the Rambo and Denavit simulation, the ion temperature is initially set to $T_i = 0.1T_0$, with the electrons given a temperature of $T_e = T_0$. These high-temperature electron fluids quickly diffuse into the centre of the system, due to their higher mobility relative to the ions, and conduct heat to the ion fluids, causing the high-temperature spike. Thus, the pressure at the centre of the system is greater than in the simulation performed in this work, inhibiting further diffusion of fluid into the central cells. Ambipolar effects seem to be negligible since, as previously stated, the ion diffusion up to time $t = 240t_0$ in fig. 3.18 is almost identical to the neutral fluid diffusion shown in fig. 3.17(a). Where fig. 3.17(c) shows significant interpenetration of the two neutral fluids, the plot of density at $t = 600t_0$ in fig. 3.18 shows

stagnation of the central ionic fluids, between two dense regions containing outward-moving shocks.

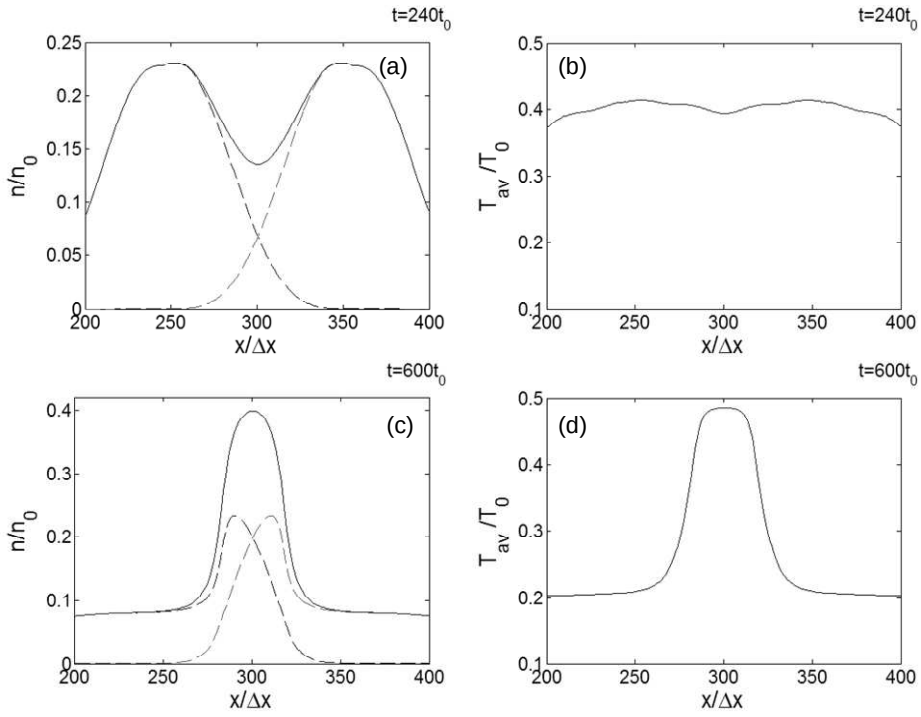

Fig. 3.17: Multi-fluid colliding plasma simulation #1 with $\eta = 6.8\times10^{-3}$. Densities and total density (a) and average temperature (b) at $t = 240t_0$; densities and total density (c) and average temperature (d) at $t = 600t_0$.

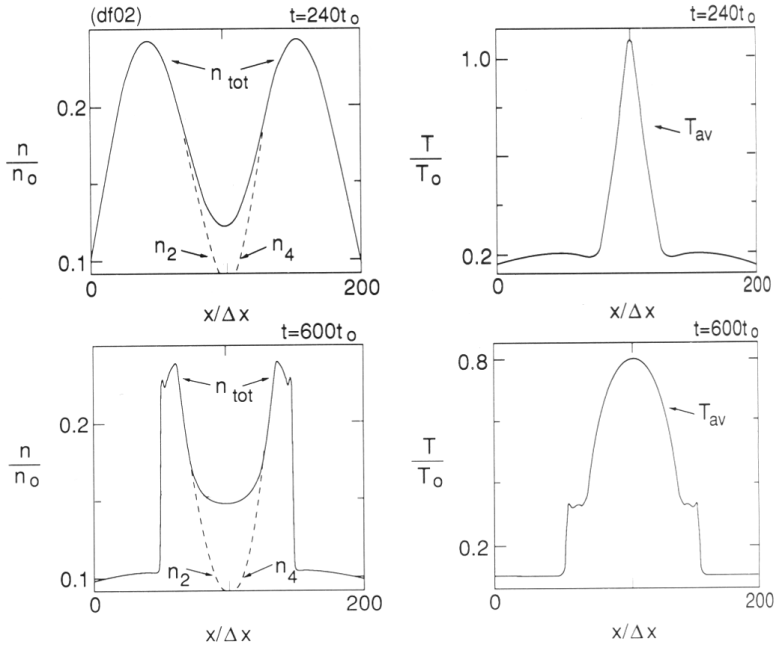

Fig. 3.18: Results from Rambo & Denavit's multi-fluid colliding plasma simulation with $\eta = 6.8\times10^{-3}$. Parameters as in fig. 3.17. Reproduced from ref. [10].

Eventual soft stagnation of the fluids in the simulation presented here is observed in the density evolution plots of fig. 3.19. The total density peak at the centre increases from time $t = 360t_0$, fig. 3.19(b), until around $t = 480t_0$, fig. 3.19(c), at which time the pressure spike at the midplane has become great enough to begin forcing diffusion of the fluid away from the centre, see fig. 3.20 for the evolution of the total pressure. The total density peak at the midplane is seen to broaden and reduce in peak magnitude from times $t = 360t_0$ to $t = 600t_0$, along with the concomitant separation of the individual fluid density peaks shown in fig. 3.19(d). The total pressure peak also broadens and reduces in magnitude from times $t = 360t_0$ to $t = 600t_0$, see figs. 3.20(c) and 3.20(d), all of which reveals the diffusion of fluid away from the midplane.

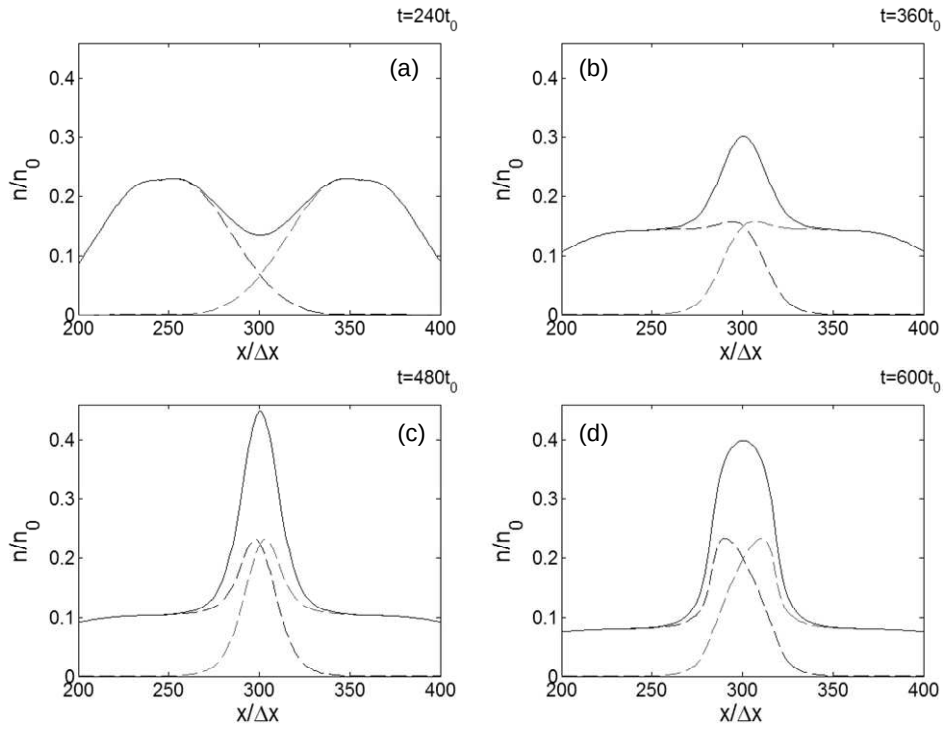

Fig. 3.19: Individual fluid densities and total density at times $t = 240t_0$ (a), $t = 360t_0$ (b), $t = 480t_0$ (c), and $t = 600t_0$ (d), in multi-fluid simulation #1 with $\eta = 6.8 \times 10^{-3}$.

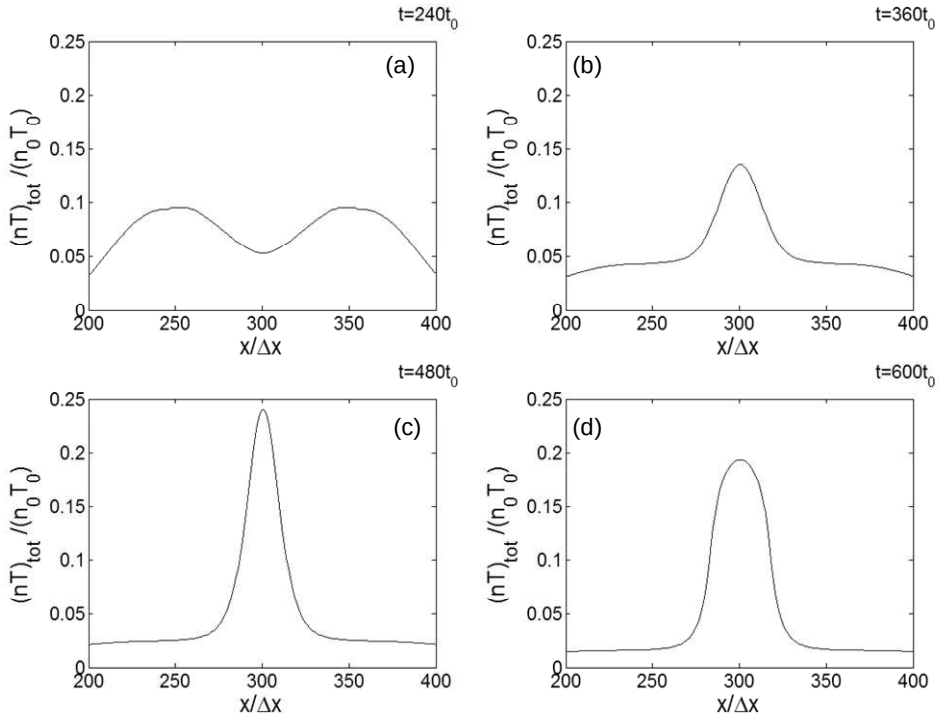

Fig. 3.20: Total pressure, $P_{tot} = n_1 T_1 + n_2 T_2$, at times $t = 240t_0$ (a), $t = 360t_0$ (b), $t = 480t_0$ (c), and $t = 600t_0$ (d), in multi-fluid simulation #1 with $\eta = 6.8 \times 10^{-3}$.

The stagnation of the fluid is also visible upon comparison of the snapshots of the momenta at the two times, $t = 240t_0$ and $t = 600t_0$, shown in fig. 3.21, revealed by the reduction of the magnitudes of the peak momenta from fig. 3.21(a) to fig. 3.21(b). Also, similar to the single fluid case, the plots show reversal of the fluid flow directions between the two times, signifying that while the two fluids initially diffuse towards the centre, at the later time $t = 600t_0$ the pressure at the midplane has inhibited the further diffusion of fluid into the centre and has begun pushing fluid outwards, away from the centre. The shocks revealed in the plots at $t = 600t_0$ of fig. 3.18, however, never form in this simulation, a result of the softer stagnation relative to the analogous simulation of Rambo and Denavit.

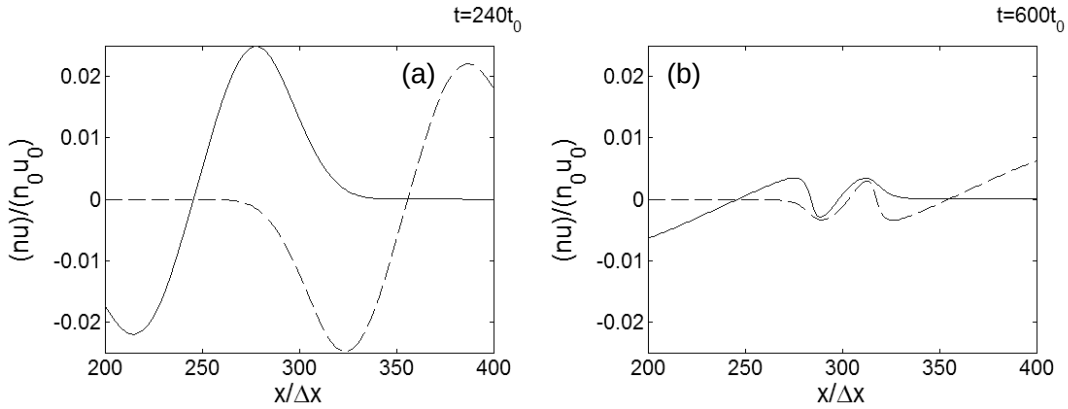

Fig. 3.21: Snapshots of the momenta at times $t = 240t_0$ (a) and $t = 600t_0$ (b), in multi-fluid simulation #1 with $\eta = 6.8\times10^{-3}$. Fluid 1 is the solid line and fluid 2 is the dashed line in each case.

Multi-fluid simulation #2 has the same input parameters and initial density profile as simulation #1, with the exception that, in this case, the *collision parameter* is one order of magnitude less: $\eta = 6.8\times10^{-4}$. The collision frequency is inversely proportional to the collision parameter, meaning there is a higher degree of collisionality in this simulation relative to the last, bringing the results closer to those of the single fluid case presented in the previous subsection with its very abrupt stagnation and formation of strong shocks. The evolution of the individual fluid densities and total density is shown in fig. 3.22 at four equally-spaced times from $t = 240t_0$ to $t = 600t_0$ inclusive, such that the plots of figs. 3.22(a) and 3.22(d) are analogous to fig. 9 of ref. [10], here reproduced as fig. 3.23. Again, significant differences are visible upon comparison of these two sets of results and are due to the same reasons as for multi-fluid simulation #1.

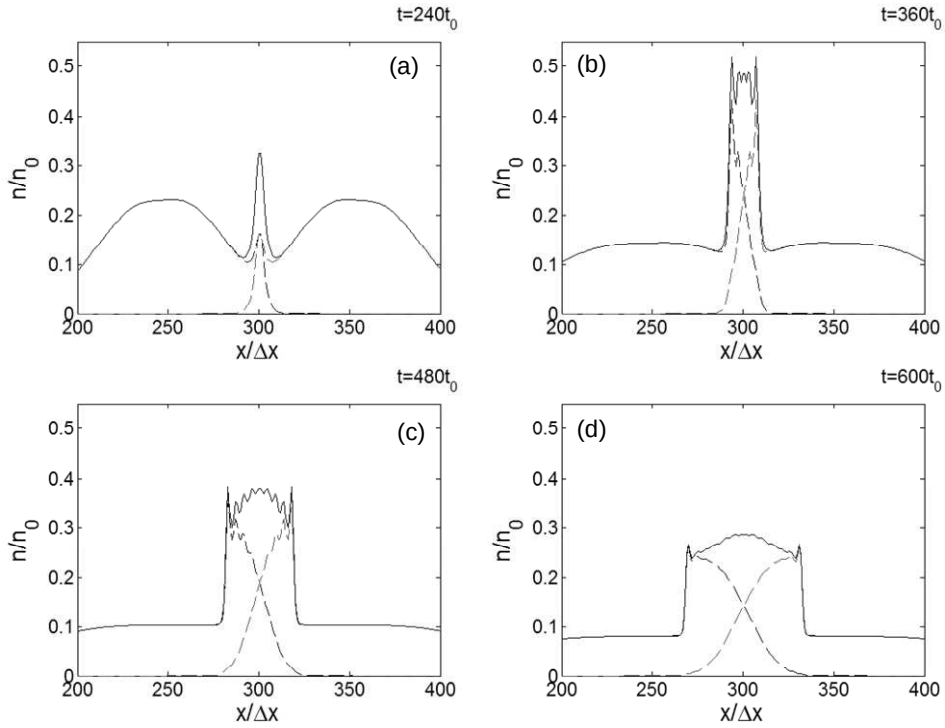

Fig. 3.22: Individual fluid densities and total density at times $t = 240t_0$ (a), $t = 360t_0$ (b), $t = 480t_0$ (c), and $t = 600t_0$ (d), in multi-fluid simulation #2 with $\eta = 6.8\times10^{-4}$.

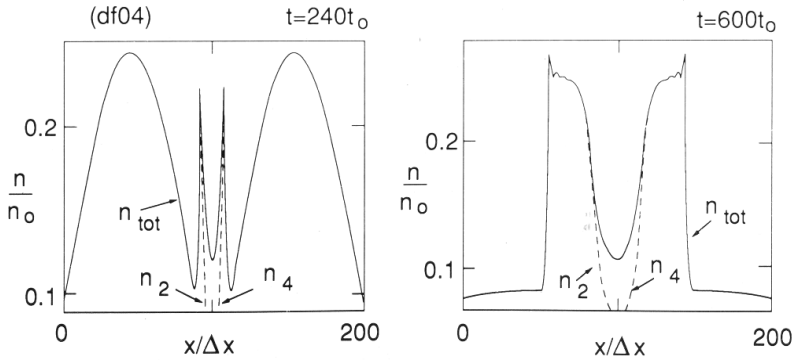

Fig. 3.23: Densities and total density from Rambo & Denavit's multi-fluid colliding plasma simulation with $\eta = 6.8\times10^{-4}$. Compare with figs. 3.22(a) and 3.22(d). Reproduced from ref. [10].

Stagnation is again less abrupt for simulation #2 than in Rambo and Denavit's equivalent high-collisionality simulation, as may be seen by comparing the density plots at time $t = 240t_0$, but, in this case, the outward-propagating shocks are clearly visible in the plots from times $t = 360t_0$ to

$t = 600t_0$, figs. 3.22(b) – 3.22(d), albeit they are closer to the centre of the system in fig. 3.22(d) than in the analogous plot of density at time $t = 600t_0$ of fig. 3.23, having been formed at a later time due to the softer stagnation. Similar to the single fluid case, the fluid regions behind the shocks exhibit oscillations due to numerical dispersion in the presence of the shocks and similar reductions of both the amplitudes of the oscillations and the sizes of the affected regions may be seen upon sequential examination of figs. 3.22(b) – 3.22(d), showing that the multi-fluid model also converges to smoother, more representative solutions as the shocks propagate outwards. The remnants of the same numerical effect are visible in the Rambo and Denavit plot of density at time $t = 600t_0$ of fig. 3.23, where small oscillations just behind the shocks are seen. From the difference in the locations of the shocks between times $t = 360t_0$ and $t = 600t_0$, figs. 3.22(b) and 3.22(d), the average speed of propagation of the shocks is found to be $v_{shock} = 0.5v_0$, a very similar result to that of the single fluid simulation, in which the shocks were found to have a speed of $0.53v_0$.

Snapshots of the momenta and total pressure at two times, $t = 240t_0$ and $t = 600t_0$, are presented in fig. 3.24. The momentum plots, figs. 3.24(a) and 3.24(c) again reveal the stagnation of the fluids, seen by comparing the average magnitudes of the fluid regions between the locations of the peak magnitudes of both fluids, which is smaller in fig. 3.24(c). Also visible is the by now familiar reversal of fluid flow between the two times.

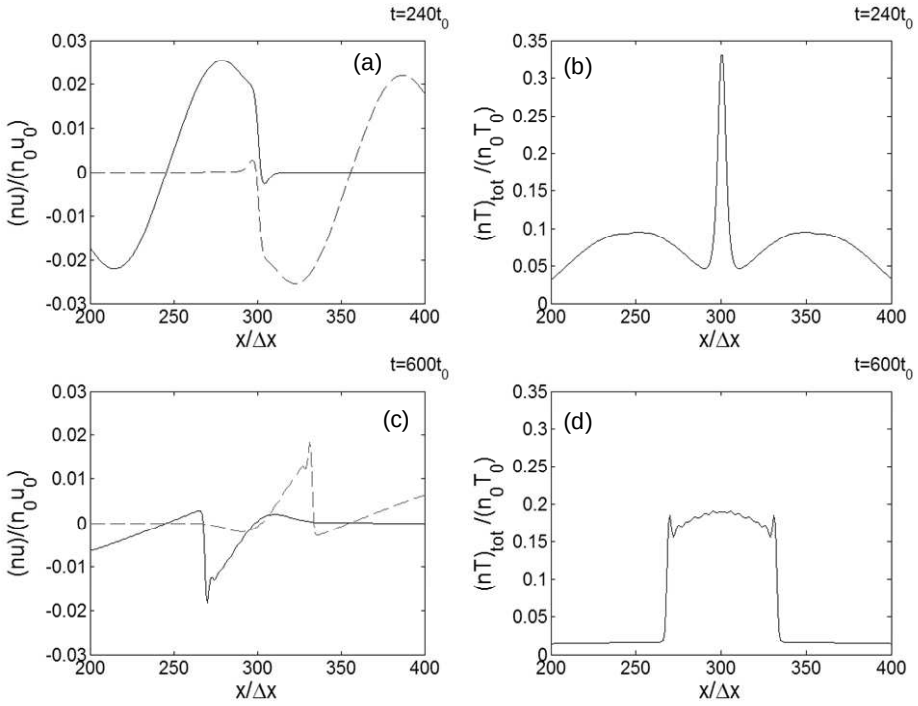

Fig. 3.24: Momenta of the individual fluids (solid line is fluid 1, dashed line is fluid 2) at times $t = 240t_0$ (a) and $t = 600t_0$ (b), and total pressures at times $t = 240t_0$ (c) and $t = 600t_0$ (d) in multi-fluid simulation #2 with $\eta = 6.8\times10^{-4}$.

Both the momentum and total pressure plots at time $t = 240t_0$, figs. 3.24(a) and 3.24(b), show very steep gradients on either side close to the midplane, and together with the confirmed presence of shocks at the later time in figs. 3.24(c) and 3.24(d), these steep gradients are clear indications that step discontinuities, i.e. shocks, are about to be formed. Expanding upon this observation, fig. 3.25 shows the total pressure evolution between times $t = 240t_0$ and $t = 315t_0$ in intervals of $25t_0$. The total pressure is seen to have reached its maximum value by time $t = 265t_0$, fig. 3.25(b), after which time the pressure spike splits into the two shocks, hinted at in fig. 3.25(c) and confirmed in fig. 3.25(d) by the numerical oscillations present in the wake of the shocks.

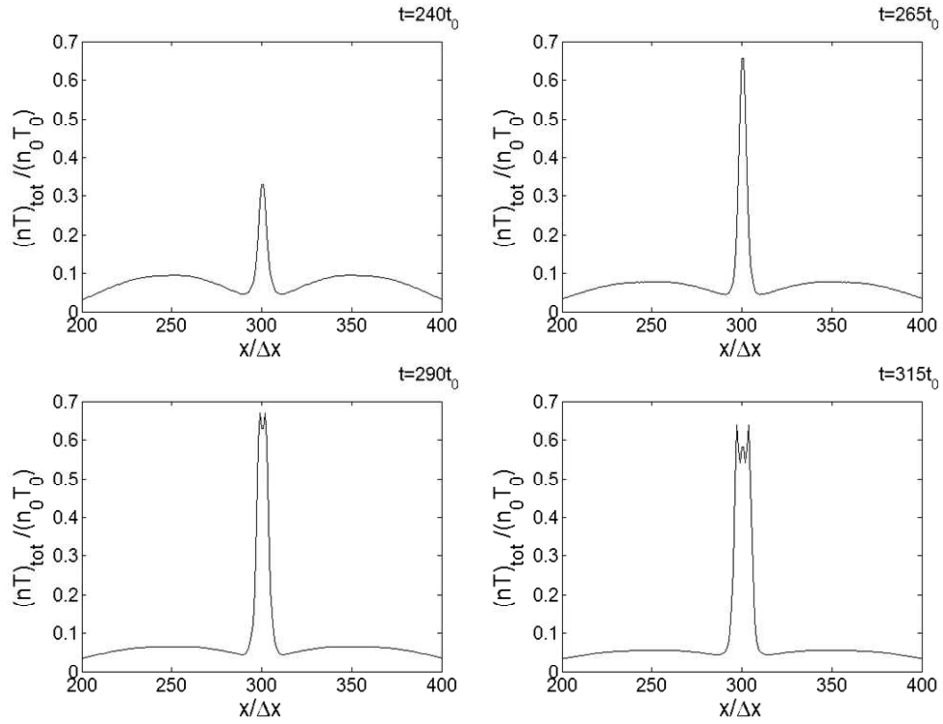

Fig. 3.25: Evolution of the total pressure profiles at times $t = 240t_0$ (a), $t = 265t_0$ (b), $t = 290t_0$ (c) and $t = 315t_0$ (d) in multi-fluid simulation #2 with $\eta = 6.8\times10^{-4}$.

Chapter 4. Conclusions and possible next steps

The results presented in chapter 3 are numerical tests of the accuracy and stability of the computational models, with the simulations initialised as closely as possible to those of Rambo and Denavit presented in refs. [6] and [10]. The first set of tests are isothermal and adiabatic simulations of neutral fluid expansions into vacuum. These simulations are initialised in such a way that the expansions are self-similar and thus possess analytical solutions, making them ideal test cases for validating the accuracy and acceptable behaviour of the discretisation scheme, especially near fluid-vacuum interfaces. In the isothermal tests, qualitative comparisons of the analytical solutions and the numerical results show good agreement in the density profiles, although small deviations from the theoretical velocity profiles and resulting momentum profiles are seen. The adiabatic simulations, which are more representative tests of the accuracy of the model due to including temperature variations, show improved agreement between computation and theory. While the computed velocity and temperature profiles deviate from the theoretical results near the fluid-vacuum interfaces, the fact that these deviations occur in regions of low density, together with the computed densities being almost indistinguishable from the analytical solutions, means that the transported quantities of momentum and pressure agree closely with theory. Quantitative estimates of the accuracy of the adiabatic simulations were obtained by calculation of the normalised root mean square deviations of the momenta and pressures in each case. The errors were calculated to be 1.30% and 0.428% for the momentum and pressure, respectively, in the first simulation with time-step, $\Delta t = 0.1 t_0$, after 200 time-steps. Upon examination of the results at a later time these errors were found to have reduced: after 300 time-steps, i.e. at time $t = 33.88 t_0$, the errors in the momenta and pressures were found to be 1.19% and 0.421%, respectively. Improved accuracy was again obtained by increasing the time-step to $\Delta t = 0.25 t_0$, thus

bringing the maximum Courant number reached close to the maximum allowed value of unity: in this case, at time $t = 33.88t_0$ the calculated errors were only 1.14% and 0.348% for the momenta and pressures, respectively.

Having shown that the model exhibits a high degree of accuracy in the elementary vacuum expansion tests, the next set of tests involved colliding plasma systems, simulated by both the single fluid and the multi-fluid models, and were compared to the results of the analogous simulations of Rambo and Denavit published in ref. [10]. The single fluid simulation shows good agreement between the two sets of results and captures the major features of the Rambo and Denavit simulation, including the formation of strong outward-propagating shocks. A small variation in the handling of the temperature transport in vacuum regions, however, causes the shocks to form at a later time in the simulation performed in this work due to less abrupt stagnation. This less abrupt stagnation proves to be a recurring theme in the multi-fluid simulations. The multi-fluid simulations presented in this work differ from the analogous simulations of Rambo and Denavit by the omission of not only electric field considerations and electron fluids, but also of thermal equilibration and heat conduction between species. Somewhat surprisingly, the lack of electric field appears to contribute little to the differing results in these particular simulations. Of greater importance is the omission of heat-conducting electron fluids, which quickly conduct heat to the low-density ionic fluids near the collision plane, causing a high-temperature spike to form at early times in the Rambo and Denavit simulations. Without this effect, the softer stagnation observed in the single fluid colliding plasma simulation is compounded due to lower pressures at the midplane. Thus, in the simulation having intermediate collisionality presented in this work, multi-fluid simulation #1, the differences are significant enough to prevent the formation of the shocks present in Rambo and Denavit's analogous simulation, due to the softer stagnation observed. In the high-collisionality simulation, multi-fluid

simulation #2, again the stagnation is less abrupt than for the Rambo and Denavit simulation, however in this case the shocks do form, albeit at a later time. Although the multi-fluid results differ significantly from the Rambo and Denavit results, the model is at least shown to be stable even in the high-collisionality case, with the shocks, physically being step discontinuities, captured in only three cells and the spurious numerical oscillations caused in their wake are shown to be quickly dampened. These two numerical effects are severe problems in computational fluid dynamic codes, often leading to major instabilities, but the relative strengths of these effects seen in the simulations presented here are well within acceptable limits and do not excessively undermine the stability of the model.

Possible extensions to the computational model here presented are numerous. Initial updates include the incorporation of temperature equilibration and thermal conduction between species, as described by Rambo and Denavit in ref. [10], which will enable heat-conducting electron fluids to be included in simulations. This will allow the results of future colliding plasma simulations to approach the analogous results of Rambo and Denavit. Of vital future importance to the development of the code is the addition to the transport algorithms of an electric field (Poisson equation) solver, such as that described by Rambo and Denavit in refs. [6] and [10]. While it has been postulated in this work that the absence of electric field considerations has little effect on the multi-fluid colliding plasma simulations presented in subsection 3.2.2, the successful incorporation of an electric field solver is imperative in order to adequately model physical plasma phenomena that are distinct from effects observed in neutral gas systems, such as ambipolar diffusion and double layers. With the inclusion of a working electric field solver, an interesting and illustrative test of the quantitative accuracy and qualitative physicality of the model would be a comparison with the observed results of a physical plasma experiment, either constrained in two dimensions in some manner thereby

approximating a one-dimensional system, or by the application of suitable geometric assumptions to the computational model, making it a so-called "1.5-dimenional" model.

The extensions to the model just described are short- to medium-term objectives. Long-term possible additions to the computational model, should the current line of research be continued, would involve the inclusion of factors not directly related to hydrodynamics, such as modelling of the laser ablation of target materials and atomic processes (ionisation, recombination, photon emission) within the plasma or due to the presence of a re-heating laser focussed on, e.g. the stagnation layer resulting from colliding plasmas. However, computer codes that model these effects have already been developed (MEDUSA, Z*), allowing for either the development of a modular code incorporating these disparate elements or simply sequential use of the various computational models to generate parameters and fluid variable (density, temperature etc.) profiles to be used as the inputs for the other codes. An extension to multidimensions is another exciting possibility, which, although challenging, would allow for "realistic" comparisons with colliding plasma experiments without having to constrain the experimental plasma system or introduce geometric assumptions into the model.

Appendix: Simulation results with Gaussian-cgs units

Presented here, without commentary, are the results from a multi-fluid colliding plasma simulation with the appropriate conversion factors applied to enable the display of the outputted fluid variables in terms of physical (Gaussian-cgs) units. This simulation uses the same multi-fluid model as for the results presented in subsection 3.2.2, with $\Delta x = \lambda_0$, $\Delta t = t_0$ and having an intermediate collisionality with $\eta = 1 \times 10^{-3}$. The initial density, velocity and temperature profiles are similar to those of the simulations of subsection 3.2.2, although with differing relative peak values; the initial profiles are displayed in the plots at time $t = 0$ of figs. A1-A3. The conversion factors utilised to convert from the normalised units used so far in this work to Gaussian units are as follows:

Density: $n_0 = 10^{23}\ \mathrm{cm}^{-3}$

Velocity: $v_0 = 10^4\ \mathrm{ms}^{-1} = 10^6\ \mathrm{cms}^{-1}$

Length: $\lambda_0 = 10^{-6}\ \mathrm{m} = 10^{-4}\ \mathrm{cm}$

Time: $t_0 = \lambda_0 / v_0 = 10^{-10}\ \mathrm{s}$

Mass: $m_0 = 1\mathrm{amu} = 1 \cdot 66 \times 10^{-24}\ \mathrm{g}$

Temperature: $T_0 = m_0 v_0 = 1 \cdot 66 \times 10^{-19}\ \mathrm{J} = 1 \cdot 036\ \mathrm{eV}$

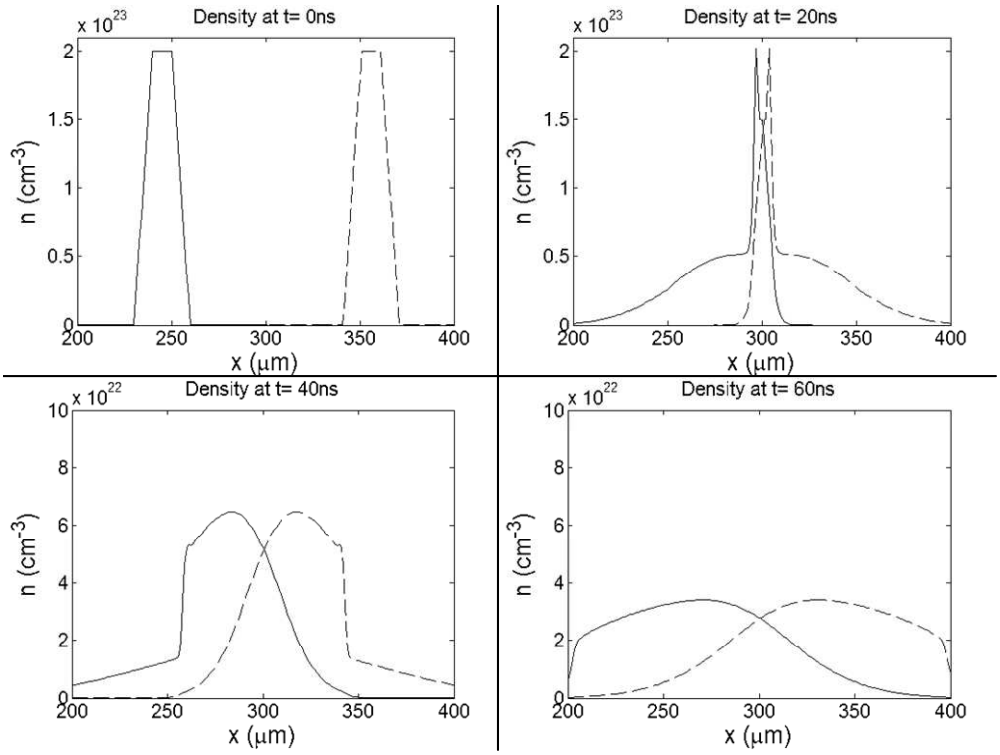

Fig. A1: Density profile evolution in a simulation with $\eta = 10^{-3}$. Fluids 1 & 2 represented by solid and dashed lines, respectively.

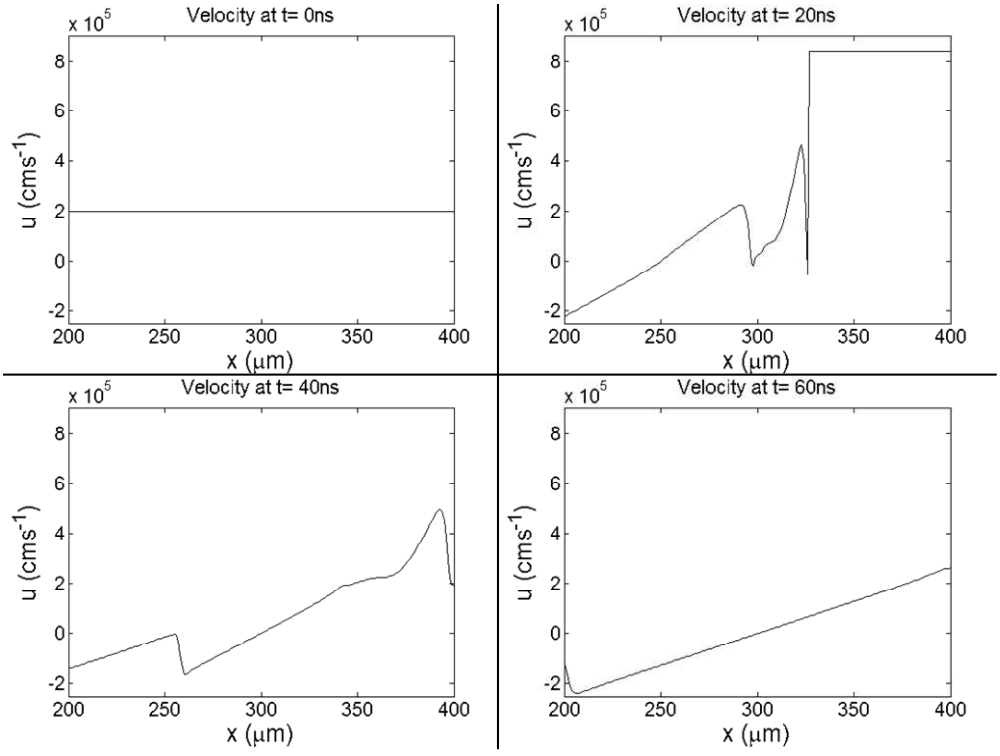

Fig. A2: Velocity profile evolution of fluid 1 in a simulation with $\eta = 10^{-3}$. The profile of fluid 2 is antisymmetric about the midplane in each case.

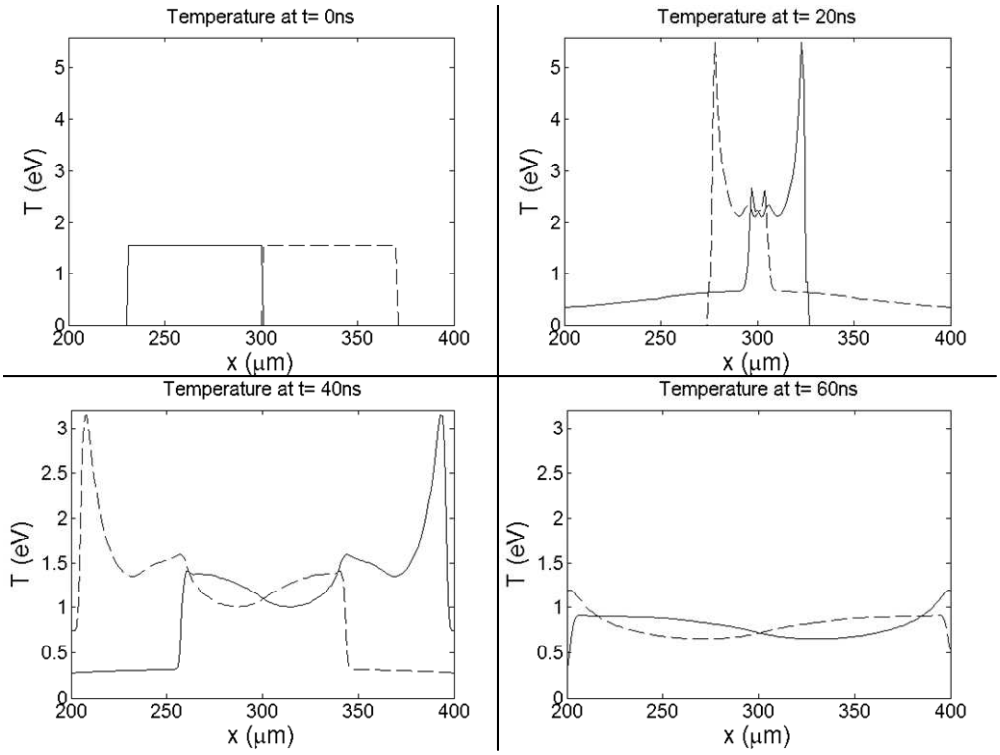

Fig. A3: Temperature profile evolution in a simulation with $\eta = 10^{-3}$. Fluids 1 & 2 represented by solid and dashed lines, respectively.

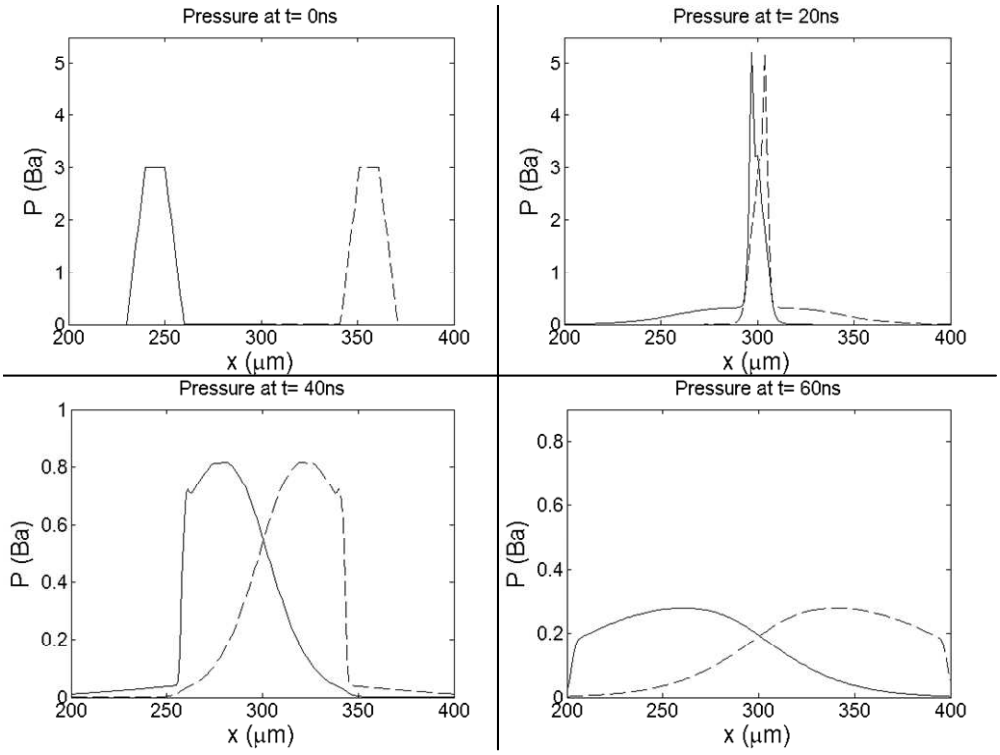

Fig. A4: Pressure profile evolution in a simulation with $\eta = 10^{-3}$. Fluids 1 & 2 represented by solid and dashed lines, respectively.

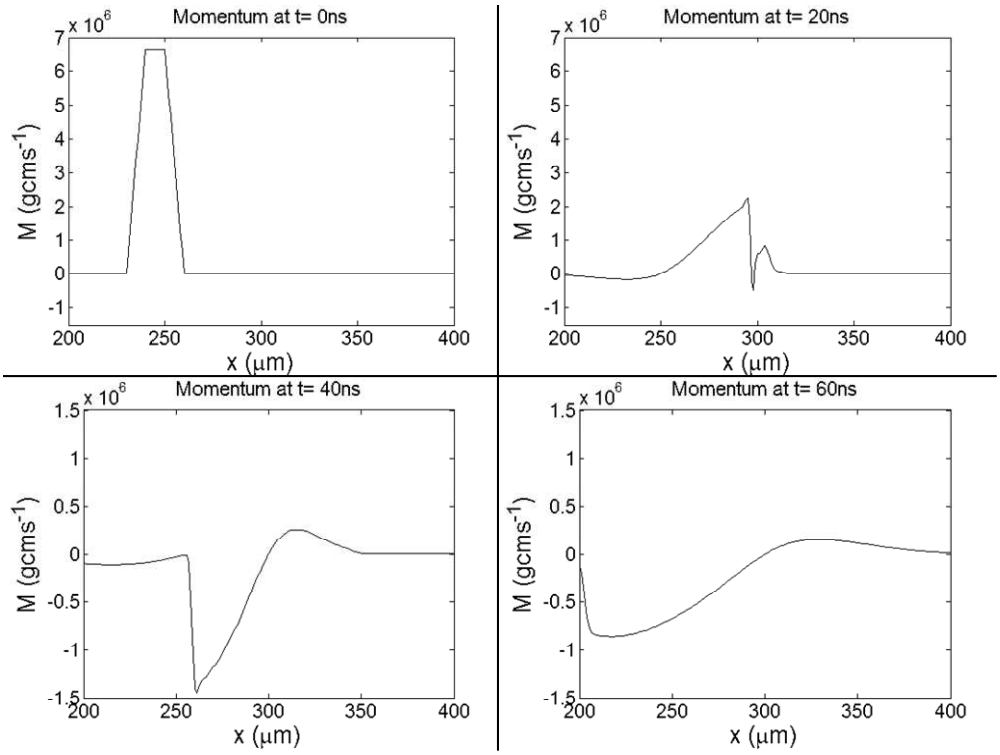

Fig. A5: Momentum profile evolution of fluid 1 in a simulation with $\eta = 10^{-3}$. The profile of fluid 2 is antisymmetric about the midplane in each case.

Bibliography

[1] Chen FF. *Introduction to Plasma Physics and Controlled Fusion (2nd ed.) - Volume 1: Plasma Physics.* New York: Plenum Press; 1984.

[2] Goldston RJ, Rutherford PH. *Introduction to Plasma Physics.* Bristol: Institute of Physics Publishing; 1995.

[3] Carroll PK, Kennedy ET. "Laser-Produced Plasmas". *Contemp. Phys.* 1981; **22**; 61- 96.

[4] Anderson JD. *Computational Fluid Dynamics: The basics with applications*. Singapore: McGraw-Hill, Inc.; 1995.

[5] Laney CB. *Computational Gasdynamics*. Cambridge: Cambridge University Press; 1998.

[6] Rambo PW, Denavit J. "Fluid and Field Algorithms for Time-Implicit Plasma Simulation". *J. Comput. Phys.* 1991; **92**; 185- 212.

[7] Boris JP, Book DL. "Flux-Corrected Transport I. SHASTA, A Fluid Transport Algorithm That Works". *J. Comput. Phys.* 1973; **11;** 38- 69.

[8] Boris JP, Book DL, Hain K. "Flux-Corrected Transport II: Generalisations of the Method". *J. Comput. Phys.* 1975; **18**; 248- 283.

[9] Boris JP, Book DL. "Flux-Corrected Transport. III. Minimal-Error FCT Algorithms". *J. Comput. Phys.* 1976; **20**; 397- 431.

[10] Rambo PW, Denavit J. "Time-Implicit Fluid Simulation of Collisional Plasmas". *J. Comput. Phys.* 1992; **98**; 317- 331.

[11] Zalesak ST. "Fully Multidimensional Flux-Corrected Transport Algorithm for Fluids". *J. Comput. Phys.* 1979; **31**; 335- 362.

[12] Fromm JE. "A Method for Reducing Dispersion in Convective Difference Schemes". *J. Comput. Phys.* 1968; **3**; 176- 189.